

AD _____

Award Number: W81XWH-11-1-0769

TITLE: Quantitative Analysis of Bone Microstructure Using Tomosynthesis

PRINCIPAL INVESTIGATOR: Yener N. Yeni, Ph.D.

CONTRACTING ORGANIZATION: Henry Ford Health System, DETROIT MI 4822-3450

REPORT DATE: October 2012

TYPE OF REPORT: Annual

PREPARED FOR: U.S. Army Medical Research and Materiel Command
Fort Detrick, Maryland 21702-5012

DISTRIBUTION STATEMENT: Approved for Public Release;
Distribution Unlimited

The views, opinions and/or findings contained in this report are those of the author(s) and should not be construed as an official Department of the Army position, policy or decision unless so designated by other documentation.

REPORT DOCUMENTATION PAGE				Form Approved OMB No. 0704-0188	
Public reporting burden for this collection of information is estimated to average 1 hour per response, including the time for reviewing instructions, searching existing data sources, gathering and maintaining the data needed, and completing and reviewing this collection of information. Send comments regarding this burden estimate or any other aspect of this collection of information, including suggestions for reducing this burden to Department of Defense, Washington Headquarters Services, Directorate for Information Operations and Reports (0704-0188), 1215 Jefferson Davis Highway, Suite 1204, Arlington, VA 22202-4302. Respondents should be aware that notwithstanding any other provision of law, no person shall be subject to any penalty for failing to comply with a collection of information if it does not display a currently valid OMB control number. PLEASE DO NOT RETURN YOUR FORM TO THE ABOVE ADDRESS.					
1. REPORT DATE October 2012		2. REPORT TYPE Annual		3. DATES COVERED 30September2011–29September2012	
4. TITLE AND SUBTITLE Quantitative Analysis of Bone Microstructure Using Tomosynthesis				5a. CONTRACT NUMBER	
				5b. GRANT NUMBER W81XWH-11-1-0769	
				5c. PROGRAM ELEMENT NUMBER	
6. AUTHOR(S) Yener N. Yeni E-Mail: yeni@bjc.hfh.edu				5d. PROJECT NUMBER	
				5e. TASK NUMBER	
				5f. WORK UNIT NUMBER	
7. PERFORMING ORGANIZATION NAME(S) AND ADDRESS(ES) HENRY FORD HEALTH SYSTEM DETROIT MI 4822-3450				8. PERFORMING ORGANIZATION REPORT NUMBER	
9. SPONSORING / MONITORING AGENCY NAME(S) AND ADDRESS(ES) U.S. Army Medical Research and Materiel Command Fort Detrick, Maryland 21702-5012				10. SPONSOR/MONITOR'S ACRONYM(S)	
				11. SPONSOR/MONITOR'S REPORT NUMBER(S)	
12. DISTRIBUTION / AVAILABILITY STATEMENT Approved for Public Release; Distribution Unlimited					
13. SUPPLEMENTARY NOTES					
14. ABSTRACT The purpose of the project is to determine the potential of Digital Tomosynthesis (DTS) for quantitative analysis of vertebral bone quality and for predicting vertebral bone fragility. The current scope, as a proof of concept study, is to compare parameters derived from DTS to those measured from microCT and test their ability to predict in vitro vertebral strength by a set of destructive tests on vertebrae from human cadavers. As of writing of this report, we characterized the DTS system for its ability to resolve features, shapes and densities using a number of man-made reference materials. We have noted that a single best scan is obtained in a scan direction oblique to the major orientation of the structure of interest but multiple orthogonal scans can provide complementary information. We noted that zero angle view of the scans provides density information complementary to the structural information obtained through the synthesis of all views. By correlating DTS-based parameters of cancellous microstructure (fractal dimension, lacunarity, mean intercept length and line fraction deviation) to those derived from microCT (distribution properties of bone volume fraction, trabecular thickness, number and separation, and degree of anisotropy) and to bone stiffness estimated from large scale finite element analysis, we demonstrated that parameters of cancellous bone microstructure derived from DTS correlate with those derived from microCT and increase prediction accuracy of bone stiffness over bone mass alone. As such, we produced strong evidence that the "concept" being explored, i.e., that quantitative analysis of bone quality using DTS is feasible. Current efforts are focused on i) examination of the information content that is represented in DTS parameters and the nature of the agreement and disagreement between microCT and DTS parameters in order to understand how predictive accuracy of DTS may be increased, and ii) mechanical testing of vertebral bodies. As future work, we are in process of integrating multiple scans (multiple orientation or multiple anatomic views) and multi-slice analysis of DTS images as well as large scale finite element analysis of whole vertebral bodies to examine the extent to which DTS can predict fracture under different modes of loading (eg. uniaxial vs wedge).					
15. SUBJECT TERMS Vertebral fracture, digital tomosynthesis, image analysis, cancellous bone texture, mcirostructural heterogeneity, osteoporosis					
16. SECURITY CLASSIFICATION OF:			17. LIMITATION OF ABSTRACT	18. NUMBER OF PAGES	19a. NAME OF RESPONSIBLE PERSON
a. REPORT	b. ABSTRACT	c. THIS PAGE			USAMRMC
U	U	U	UU	34	19b. TELEPHONE NUMBER (include area code)

TABLE OF CONTENTS

	<u>Page</u>
Introduction.....	4
Body.....	4
Key Research Accomplishments.....	30
Reportable Outcomes.....	31
Conclusion.....	32
References.....	32
Appendices.....	34

INTRODUCTION

Accuracy in the prediction of osteoporotic fracture risk using bone mineral density alone is limited. Experiments using laboratory scale imaging devices (microCT) on cadaver bones show that parameters that quantify the heterogeneity of the cancellous bone microstructure are especially useful for predicting vertebral strength. However, measurement of bone microstructure in a clinical setting is difficult and, when possible, is generally limited to easily accessible extremities. Digital tomosynthesis (DTS) is a clinically available imaging technique that can produce multiple planar images of an object with high resolution, as if the object was physically sliced before imaging. The objective of the current project is to determine the potential of DTS for quantitative analysis of vertebral bone quality and for predicting vertebral bone fragility. As a part of this evaluation, parameters derived from DTS are compared to those measured from microCT and their ability to predict in vitro vertebral strength is examined by a set of destructive tests on vertebrae from human cadavers. Methods of fractal, lacunarity, mean intercept length and line fraction deviation analyses are used to quantify cancellous microstructure from DTS images. The strength of the vertebrae will be measured using a loading mode that will generate a wedge-shaped fracture as seen in clinical vertebral fractures. If DTS provides structural information sufficiently detailed compared to the microCT gold standard or that significantly correlates with the strength, the development of this concept into a clinical screening process will be pursued through further refining and testing.

BODY

Task 1. *Retrieval of 20 cadaveric human fresh-frozen thoraco-lumbar vertebrae from tissue banks and body donation programs (Months 1-4):*

1a. Review and activation of tissue collection protocols by the donation program (Months 1-2).

1b. Collection and shipment of the vertebrae (Months 2-4)

Approval of the institutional review board (IRB 6688) for the project was obtained and submitted to the USAMRMC Office of Research Protections (ORP), Human Research Protection Office (HRPO) for review along with a claim of exemption from review to use preexisting cadaveric vertebrae. The statement that the project may proceed with no further requirement for review by the HRPO was received prior to the beginning of the supported period. In accordance with this notification (HRPO Log Number A-16751), newly retrieved vertebrae as well as previously existing deidentified cadaveric vertebrae are used.

We identified 40 fresh-frozen thoraco-lumbar vertebrae from 10 subjects previously collected through approved protocols and allocated them to the project. In addition, we established tissue collection protocols with the National Disease Research Interchange (NDRI), the Anatomical Donations Program of the University of Michigan and Platinum Training. Seven spines were supplied by NDRI and nine by Platinum Training (total 16 new spines).

Currently, we have completed collection of tissue.

Task 2. *Refinement of Digital Tomosynthesis (DTS) scan parameters (Months 1-4):*

2a. In order to have reference materials that resemble cancellous bone but with estimated properties, prepare wire-mesh references with a wire thickness of 50 μ m and varying mesh density with wire separation in the order of 1mm and varying out-of-plane separation. (Month 1)

2b. Perform a series of DTS scans on these references using variations of tube angle, number of projection images, number of reconstructed planes and the incident exposure for each projection. (Months 1-3)

2c. Perform μ CT on reference materials. (Months 1-3)

2d. Determine scan parameters that produce the best agreement between μ CT and DTS. (Month 4)

In order to refine DTS scanning parameters, custom phantoms were created to assess the accuracy of DTS in resolution of separation, thickness, distances, in-plane and out-of-plane geometric distortion, and density linearity.

To assess the minimum spacing which may be resolved by DTS, six phantoms were created comprised of equally spaced stacked squares of radiopaque aluminum and radiolucent acrylic at 350, 300, 250, 200, 150, and 100 μ m nominal spacing, as measured by micrometer during phantom preparation (**Figure 1a**). The squares were clamped and bound at the edges using epoxy to create a solid construct. The resulting cross-sectional banding pattern thickness and frequency is comparable to human trabecular bone. To assess the

minimum thickness which may be resolved by DTS, another set of six phantoms was created with thin radiopaque aluminum layers (nominally 25, 60, 75, 90, 115 and 120 μm as manually measured from micro-CT images) bound between thick (1.5 mm) layers of radiolucent acrylic (**Figure 1b**).

Density linearity phantoms were created using serial dilutions of 28.2% (282 mg/ml) organically bound iodine in the form of iohalamate meglumine, an ionic contrast agent. Nominal concentrations of 282, 141, 70.5, 35.25, 17.63, and 8.81 mg/ml organically bound iodine, as well as air and water, were placed in a sealed well plate (**Figure 1c**).

For demonstration of anisotropic and edge-enhanced characteristics of DTS, a nylon sphere (**Figure 1d**) and cylinder (**Figure 1e**) were included in the phantom tray. To aid in measuring true voxel size in the reconstructed volume, a geometric accuracy phantom was created using four 1 mm beads, placed in four corners at 35 mm apart (**Figure 1f**). An embedded human vertebra was also included in the phantom as a realistic reference material (**Figure 1g**).

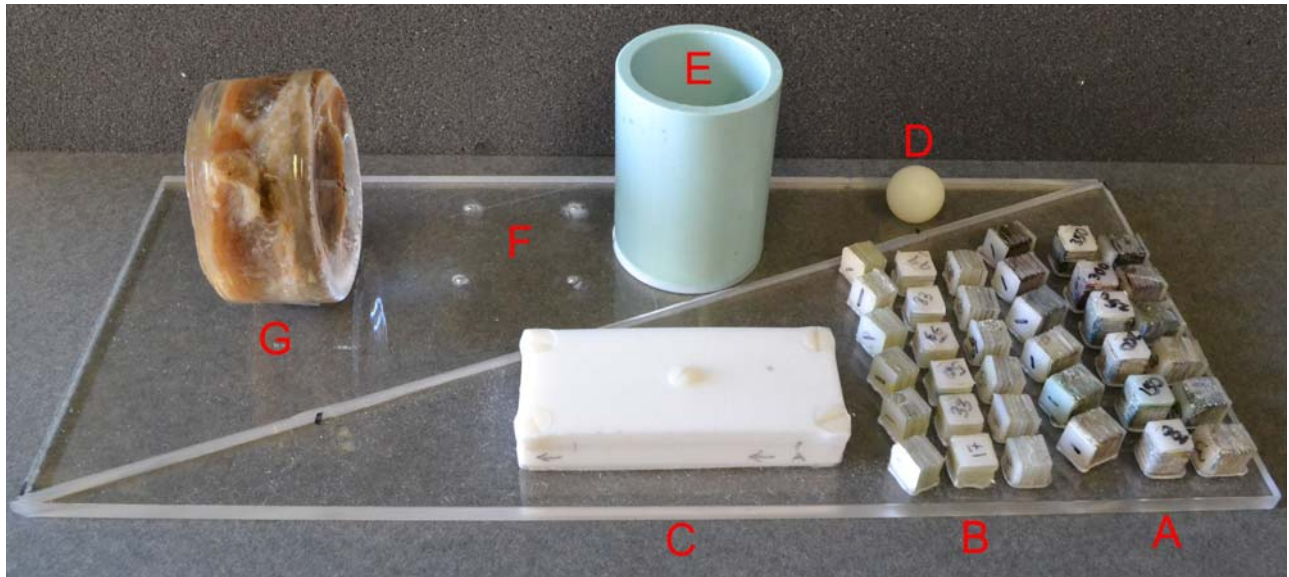


Figure 1: Tray of phantoms to assess DTS resolution, geometric distortion, and density linearity.

An aluminum grid panel with hollow evenly spaced cells with known dimensions (12.7 x 12.7 x 12.7 mm, **Figure 2**) was used to examine geometric distortion and uneven signal distribution within the reconstructed DTS images.

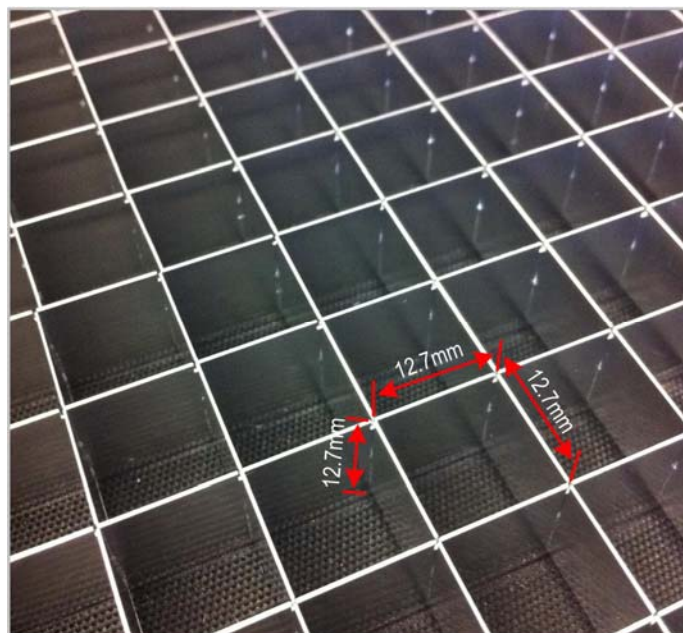


Figure 2: Aluminum grid panel phantom to assess geometric distortion in x, y and z directions.

Density linearity phantoms

In each of 5 scanning sessions, DTS scans and planar digital radiographs were performed on the sealed wells containing serial dilutions of iodine solution. As DTS scans were performed with the phantom tray oriented in 3 directions, the density phantoms were scanned a total of 3 times per session, allowing assessment of session-to-session variability as well as within-session variability. A single radiograph was taken in each session.

Images were inverted for white on black presentation, and a cylindrical selection was drawn at the center of each well. Average gray value was measured for each well at a single orientation for each session. Only the central 8 mm of each well was analyzed to avoid a darker region of edge enhancement at the perimeter of each 10 mm diameter well, which is due to a high-pass filter applied in the direction of tomographic acquisition. To assess within-session variability, measurements were repeated at three orientations per session. Radiographs were similarly analyzed by recording average gray values within an 8 mm circle for each well.

Spacing phantoms

Spacing phantoms were scanned using microcomputed tomography (micro-CT) and reconstructed at 22 μm isotropic voxel size. Micro-CT images were cropped to include only the phantom, and were resliced to expose a central cross section representing the phantom's banding pattern. DTS scans were performed on the phantom tray oriented in 3 directions: parallel, perpendicular, and at 22.5° oblique to the scanning direction (**Figure 3**). As there were 2 sets of spacing phantoms (oriented in line and at 22.5° to length of the tray) for in-plane assessment, the 3 scanning directions allowed the phantoms to be scanned a total of 4 different angles relative to the scanning direction (0°, 22.5°, 67.5° and 90° to the scanning direction).

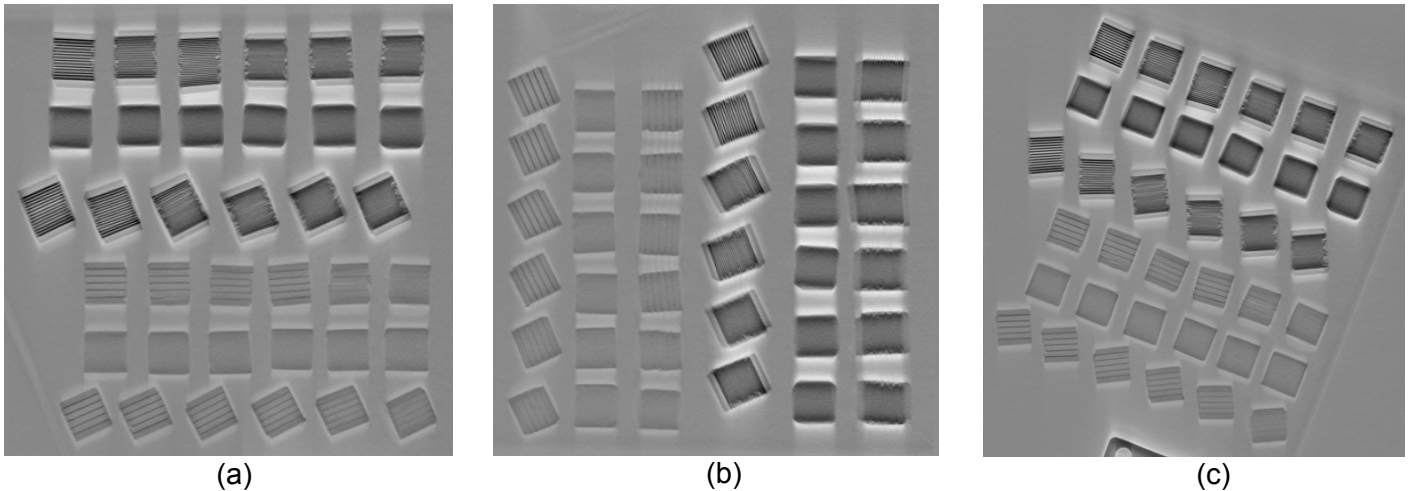


Figure 3: DTS reconstructions of spacing and thickness phantoms oriented parallel (a), perpendicular (b), and 22.5° (c) to the scanning direction

Visual Analysis of DTS Spacing Phantom Images

DTS images of spacing phantoms were visually assessed for presence of a banding pattern. A central cross-sectional slice from each phantom was viewed at 200% magnification with display range set to the full pixel value range of the image.

Quantitative Analysis of Microcomputed Tomography and DTS Spacing Phantom Images

A vertical line with thickness of approximately 2 mm was drawn between the top aluminum layer and the bottom aluminum layer (**Figure 4**). A mild median filter with a kernel of 2 was applied to the image to reduce noise. A gray value profile was plotted along the vertical line, which was processed using a Fast Fourier Transform (FFT) to assess frequency of the banding pattern.

The resulting frequency-domain plot was assessed to identify maximum peaks representing frequency magnitude of the banding pattern. Average layer thickness was calculated as $0.5 \cdot (1/\text{frequency})$ at the maximum peak. The peak location and thickness was considered a gold standard by which to compare subsequent analyses of DTS images. The same procedure was performed on DTS phantom scans from a single, randomly-chosen scanning session.

Textural information was visually present in phantoms 250 μm and below which was not identified in FFT

analysis, so mean intercept length (MIL) and line fraction deviation (LFD) analyses were performed. A single cross-section from the six phantoms at the 0° angle was cropped from the DTS reconstruction. MIL and LFD analyses were performed using a custom MATLAB script (Sander and Barocas, 2009). From MIL analysis, maximum MIL (MIL.Max) and its angle (MIL.MaxAngle) were recorded, as well as average MIL (MIL.Av), degree of MIL anisotropy (ratio of maximum to minimum MIL, MIL.DA), and standard deviation of MIL (MIL.SD). From LFD analysis, maximum LFD (LFD.Max) and its angle (LFD.MaxAngle), minimum LFD (LFD.Min), average LFD (LFD.Av), degree of LFD anisotropy (ratio of maximum to minimum LFD, LFD.DA), and standard deviation of LFD (LFD.SD) were recorded. In addition, similar parameters were recorded when an ellipse was fit to LFD measurements (LFD.EllipseMax, LFD.EllipseMin, and LFD.EllipseMaxAngle). LFD and MIL parameters allow quantification of pattern directionality in the phantom images. LFD is typically more sensitive to anisotropy than MIL, as the method calculates the fraction of bright pixels in a grayscale image along many closely packed lines at various angles, rather than counting intersections at various angles in a binarized image (Geraets, 1998).

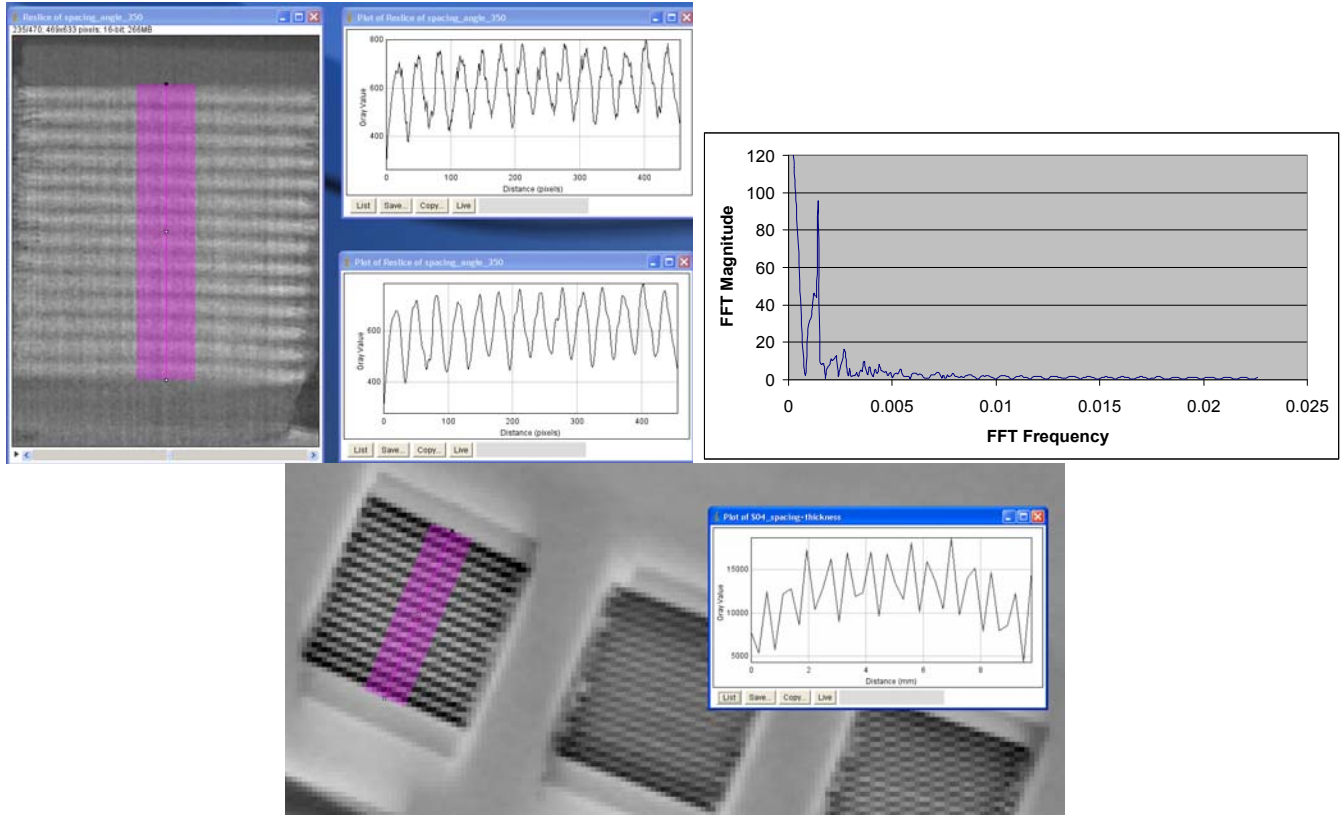


Figure 4: Creating line profile for Fast Fourier Transform from filtered micro-CT reconstruction (upper left). In the above plot, a peak was identified at 351.23 μm (upper right). The same procedure was repeated for DTS images (bottom center).

Fractal dimension and lacunarity were calculated from the same images using FracLac (Karperien, 2007). The box counting method (Fazzalari and Parkinson, 1996; Plotnick et al., 1996) was used to assess fractal dimension, a measure of image complexity which uses the difference between maximum and minimum gray values to describe how a pattern's details change with scale. Lacunarity, a measure of translational invariance, was also calculated. Both methods work together to characterize the existence of patterns within an image.

Thickness Phantoms

Thickness phantoms were scanned using microcomputed tomography and reconstructed at 10 μm isotropic voxel size. Micro-CT images were cropped to include only the phantom, and were resliced to expose a central cross section representing the phantom's banding pattern. The two sets of in-plane thickness phantoms (oriented in line and at 22.5° to length of the tray) were also DTS scanned in three orientations as described above, yielding 4 different angles relative to the scanning direction (0°, 22.5°, 67.5° and 90°; **Figure 3**).

Visual Analysis of DTS Thickness Phantom Images

DTS images of thickness phantoms were visually assessed for presence of aluminum layers separated by

plastic. A central cross-sectional slice from each phantom was viewed at 200% magnification with display range set to the full pixel value range of the image.

Quantitative Analysis of Microcomputed Tomography and DTS Thickness Phantom Images

The same FFT, morphometric and textural analyses as previously described were performed on micro-CT and DTS images of the thickness phantoms.

Aluminum grid panel phantom

The aluminum grid panel was scanned in four angular orientations relative to the scanning direction (**Figure 5**; 0°, 15°, 22.5° and 45°). Each scan generated a stack of 11 reconstructed image slices with 1 mm spacing between each slice. Two rectangular regions of interest (ROI: L1 and L2) with 500 pixel width and maximum length allowable within each the DTS image were analyzed for the gray value profiles, covering approximately 60-70% of examined image area.

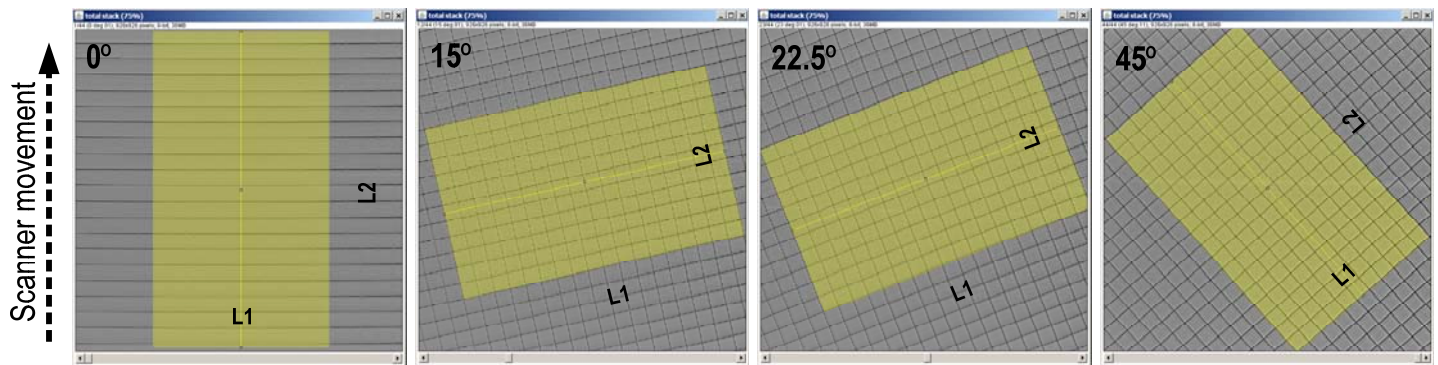


Figure 5: Aluminum grid panel was imaged at four angular orientations (0°, 15°, 22.5° and 45°) respective to the scanning movement. Each angular orientation constituted of 11 DTS slices that were spaced 1 mm between slices. The gray value profile of each image slice was measured at two principal orientations L1 and L2 (yellow boxes).

This task is complete.

Task 3. Microcomputed tomography (μ CT) (Months 5-6):

3a. Microcomputed tomography scanning/reconstruction of individual vertebral bodies at 30 micrometer voxelsize using a calibrated radiographic reference. (Month 5)

3c. Preparation of regions of interest, segmentation and quantification of average and standard deviation of conventional micro-CT parameters using specialized CT-analyzer software: bone volume fraction, bone surface to volume ratio, trabecular number, thickness and separation, structure model index, connectivity and anisotropy. (Month 5)

3d. Preparation of regions of interest and calculation of fractal dimensions and lacunarity. (Months 5-6)

3e. Preparation of regions of interest, segmentation and calculation of line fraction deviation. (Month 6)

We have previously noted that calculations of microstructural properties are affected by the voxel size used in micro-CT scanning and image reconstruction (Kim et al., 2004). The maximum resolution that can be achieved during a micro-CT scan is affected by the size of the object; larger vertebrae allow for larger minimum voxel size (resulting in lower resolution). In order to avoid a potential confounding effect of vertebral size (through voxel size) on calculated parameters, we determined a minimum voxel size that can be used for all vertebrae in the study by measuring vertebral dimensions of the actual specimens, either on the specimen using a caliper or on images captured from pilot micro-CT views. We determined for the first 40 vertebrae (T6, T8, T11 and L3 vertebrae from 5 female and 5 male cadavers; Age 63-90 years) that 45 micrometers is the minimum voxelsize that can be used for all the samples. Large scale finite element models of cancellous bone based on micro-CT images with 50 micrometer voxelsize achieved good agreement with experimentally measured stiffness in previous work (Hou et al., 1998) indicating that the cancellous microstructure of vertebral bone is sufficiently resolved at this resolution.

The in-house micro-CT system used in the project is built on the principles of an earlier in-house system previously described in detail (Reimann et al., 1997). The presently operating system uses a Kevex 16-watt x-ray source with a 9-micron focal spot, a 1888x1408-pixel Varian PaxScan 2520 flat panel digital x-ray detector with

127-micron pitch, a Newport precision rotational stage, and control software running under Windows XP. Each vertebra was placed in a radiolucent tube, sealed prior to scans, and scanned using our in-house micro-CT system at a voxel size of 45 μm . In each reconstruction of whole vertebral body, the largest possible cubical volume of interest (VOI) consisting only the cancellous bone was digitally cut out using Image J (NIH, USA). The bone and non-bone phases were segmented using Microview (v2.0, GE Healthcare, Little Chalfont, UK), which is based on standard global thresholding procedures previously described and widely used (Kuhn et al., 1990; Hou et al., 1998; Yeni and Fyhrie, 2001).

For analysis of the microstructure, the segmented images were binarized. The analysis was carried out using both custom-written software (Goulet et al., 1994; Yeni et al., 2011) and commercial software (CT Analyzer, Skyscan, Kontich, Belgium). The intra-specimen mean (A_v) and standard deviation (SD) of the following microstructural properties were calculated from each binarized VOI using stereologic methods: Bone volume fraction (BV/TV), bone surface to volume ratio (BS/BV) trabecular thickness (Tb.Th), trabecular number (Tb.N) and trabecular separation (Tb.Sp). Degree of anisotropy (DA) was also calculated using the 3D Secants, configuration and star volume methods. The A_v and SD were recorded as measures of intraspecimen magnitude and heterogeneity, respectively, of a given parameter. Connectivity, structure model index and fractal dimension parameters were calculated using CT Analyzer among other properties of the microstructure.

In addition to the analyses of microstructure, we performed finite element simulations on each of the cancellous bone volumes, in order to estimate cancellous bone stiffness and trabecular stress distribution properties. This was to obtain Young's modulus (E_{FEM}), coefficient of variation of von Mises stress distribution (VMCV) and average trabecular von Mises stress per apparent uniaxial stress ($\text{VMExp}/\sigma_{\text{app}}$) in the cancellous bone, and later to build multi regression models with DTS parameters to assess prediction capability of the DTS system. Linear elastic FE models with isotropic element properties were prepared using a custom-written meshing algorithm as in previous studies (Yeni et al., 2005). Young's modulus of each bone element was assigned using an approach similar to that used by Nekkanty et al. (Nekkanty et al., 2010) resulting in the relationship:

$$E_{\text{tissue}} \text{ (MPa)} = (8020/1130.257) GL_{\text{element}}$$

where GL_{element} is the gray-level of the element and 1130.257 is the gray level corresponding to a mineral density of $1.223\text{g}/\text{cm}^3$. All elements were assigned a Poisson's ratio of 0.3. Uniaxial compression was simulated by using a displacement equivalent to an apparent strain of 0.005. The models were displaced in the superoinferior direction while the displacements in other directions were not constrained (Free-end conditions). The models were solved using a custom-written element-by-element pre-conjugated gradient solver as in previous studies (Hou et al., 1998; Yeni et al., 2005). Apparent modulus of cancellous bone was calculated using nodal reaction forces, the apparent surface area of the sample and the input apparent strain. The average and standard deviation of trabecular von Mises stress were calculated for the entire sample.

What remains to be done in this task is the analysis of line fraction deviation (LFD) from micro-CT images. We now have automated this measurement during analysis of DTS images (see below and also the abovementioned phantom studies) and are able to batch-process image sets for this analysis. We can not only analyze selected sections from the image as was originally planned but can also process an entire series of slices within a single micro-CT volume. We expect that this will allow for a more rigorous examination of the agreement between the micro-CT and DTS images. We do not expect difficulty in completion of this sub-task.

As an extension to this task, we are constructing a second set by selectively including vertebrae that are small enough to be scanned at 30-35 micrometers. This will likely result in a thoracic-only set with a large range of donor age. Once complete, the results will be complementary to the initial set of 40 vertebrae.

Task 4. Digital Tomosynthesis (DTS) of vertebrae (Months 7-9):

- 4a. DTS scanning of vertebral bodies using the SonialVision Safire II system (Shimadzu Co., Kyoto, Japan), with the superoinferior axis as the axis of image rotation. Scans with the coronal and sagittal views centered at zero degree angle will be obtained. (Month 7)*
- 4b. Preparation of regions of interest and calculation of fractal dimensions and lacunarity. (Months 7-8)*
- 4c. Preparation of regions of interest, segmentation and calculation of line fraction deviation. (Month 8)*

The vertebral bodies were scanned in coronal and sagittal views using the Shimadzu Sonialvision Safire II tomosynthesis system (Shimadzu, Kyoto). For each bone, 74 radiographic tomosynthesis images were captured over 2.5 seconds at 65 kV and 250A and then reconstructed with image slice thickness of 1mm. Central coronal DTS image for each vertebra was chosen for the image analyses, where the largest possible rectangular cancellous bone region of interest (ROI) was selected for the fractal analysis (fractal dimension and lacunarity), MIL (mean intercept length) and LFD (line fraction deviation) analyses (**Figure 6**).

Fractal analysis was performed on images with no pre-processing. Because recognition of trabecular structures is important for the MIL and LFD analyses, images were processed to enhance extraction of trabecular structures within the image texture. Three types of processing methods were examined:

- i) USM - unsharp mask (USM) filter sharpened without binarization (i.e. grayscale)
- ii) Bin.Csv – conservative binarization by use of weak convolution and high pass filters
- iii) Bin.Ag - aggressive binarization by use of strong convolution and high pass filters

The filtering processes were performed using Photoshop (Adobe Systems Inc, San Jose, California) and ImageJ (NIH, Bethesda, Maryland).

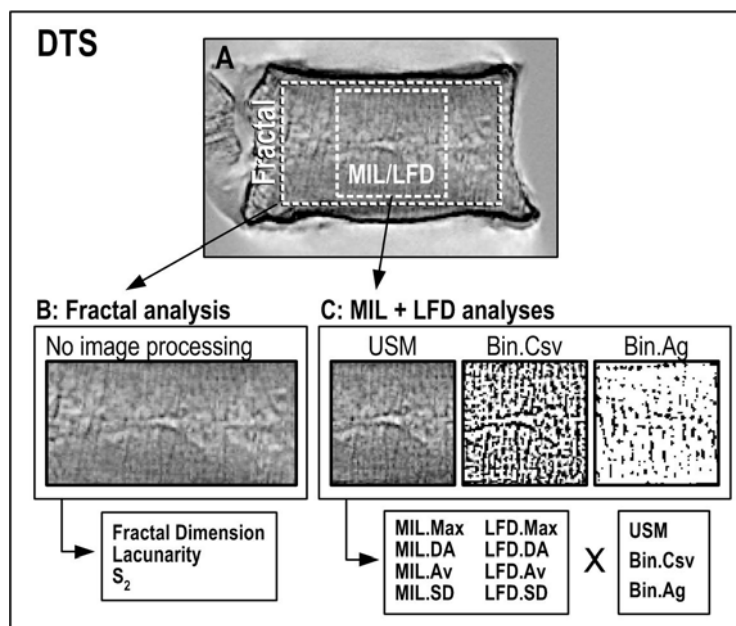


Figure 6: A) A typical DTS image segment used for the analyses. There were two types of ROI; B) Fractal dimension, lacunarity and S_2 were calculated through fractal analysis without image pre-processing. C) MIL and LFD parameters (Max, DA, Av and SD of MIL and LFD) were calculated for each of the three types of image pre-processing methods (USM, Bin.Csv and BIN.Ag).

Fractal analysis – Using box count fractal analysis method (Fazzalari and Parkinson, 1996; Plotnick et al., 1996), fractal dimension and mean lacunarity were obtained by use of FracLac 2.5 plugin (Karperien, 2007) of ImageJ (NIH, Maryland). The box count method uses a series of sequentially reducing box size grids on the image to sample the local difference between the maximum and minimum gray values in each box region. As a secondary derivative measure of lacunarity, a slope of lacunarity against box size value was also calculated (S_2).

MIL and LFD analyses – We have performed both MIL and LFD analyses using custom MATLAB codes (Mathworks, MA), calculating MIL and LFD values for each 1 degree increment over 360 degrees (Sander and Barocas, 2009). The MIL and LFD values were polar plotted (**Figure 7**) and mean (Av), standard deviation (SD), maximum (Max) and degree of anisotropy (DA) of MIL and LFD were obtained for each DTS image.

This task was completed and the data were analyzed as planned. As an extension of this task, we performed additional DTS scans, with the image rotation axis transverse or oblique to the supero-inferior axis in addition to those parallel to the supero-inferior axis (zero degree angle). In addition, we developed the capability to automatically batch-process a large number of images which allows us analysis of multiple sections in a DTS scan. With these additional data, we expect that we will be able to better address the research topic.

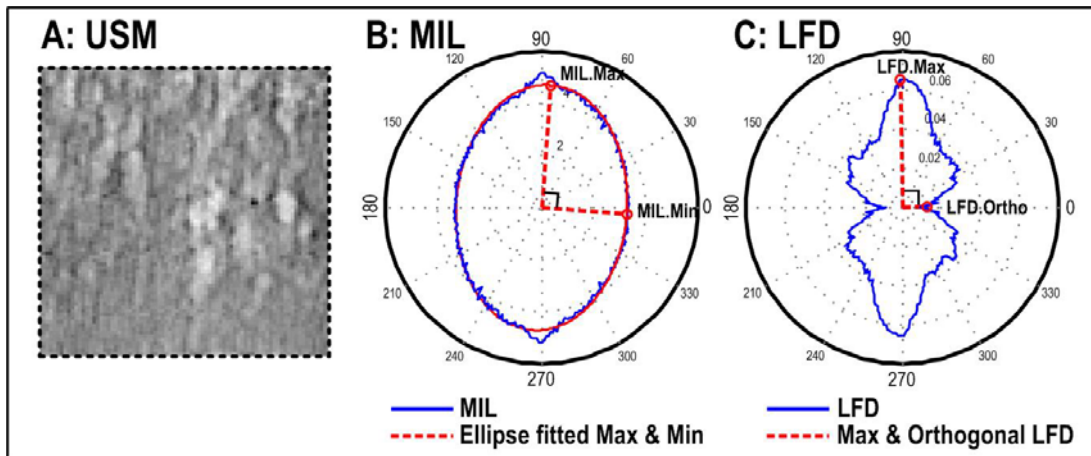
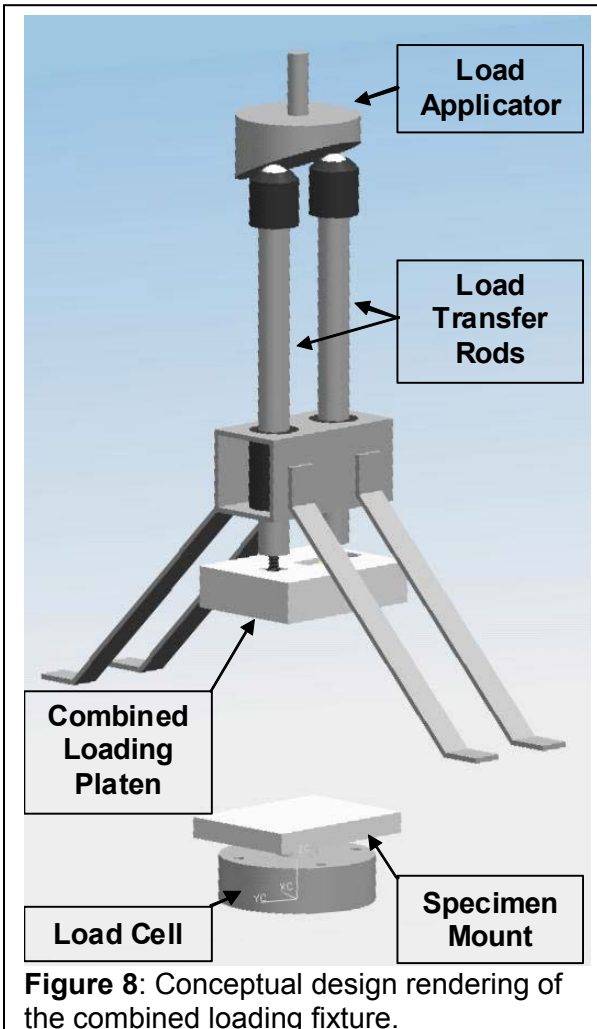


Figure 7: A) An example of a DTS image that generated polar plots of B) MIL (mean intercept length) and C) LFD (line fraction deviation). Note how overall orientations of the polar plots correspond to that of the trabecular texture in (A). Dotted red lines represent the principal components in MIL and LFD. The degree of anisotropy (DA) was calculated from the ratio of maximum to secondary principal component where MIL.DA was from MIL.Max/MIL.Min and LFD.DA was from LFD.Max/LFD.Ortho.

Task 5. Mechanical testing of vertebral bodies (Months 10-11)

5a. Non-uniform compression testing of vertebral bodies using a materials test machine (8501M, Instron Inc., MA). Determine vertebral strength as the maximum load during fracture. (Months 10-11)

5b. Reduction of mechanical test data. (Month 11)



The mechanical testing fixture and protocol were designed to apply non-uniform loading conditions to the specimen vertebral bodies. Specifically, the non-uniform loading would consist of uniaxial compression and a bending moment, which would simulate the loads producing a wedge fracture, often a result of heavy weight lifting. The objective of the design and protocol was to allow independent control of the compressive load and the bending moment. Previous researchers achieved combined loading via wedged load platens (McDonnell et al., 2010), multi-arm hydraulic systems (Whealan et al., 2000), and robotic arm (Buckley et al., 2007). We produce the requisite loading via an axial and rotary actuator. The axial actuator control applies the compressive loading condition while the rotary actuator control applies the bending loading.

During the study period, we started by designing and fabricating a prototype combined loading fixture to proveout the concept – **Figure 8** is a conceptual design rendering of the prototype. The upper load applicator has an inclined surface which, when rotated, directs one of the load transfer rods downward and the other upward. This rotates the combined loading platen and imparts bending to the specimen mounted to the specimen mount. Axial displacement of the load applicator directs both load transfer rods downward simultaneously and imparts specimen compression. Testing during the prototype trials consisted of applying compression, bending, and combined compression and bending to a foam test block to evaluate the combined loading fixture operation. The combined loading of the test foam blocks produced a linear load response (**Figures 9-12**).

Fabrication of the project combined loading fixture commenced after the prototype tests were complete (**Figure 13-15**). Two design changes were incorporated in the final design. The first design change consisted of reducing the angle of the inclined surface on the load applicator from 22° to 11° which reduced the maximum bending angle placed on the vertebral body to 5°. The second design change was to include a flat section on half of the load applicator, with the other half inclined at the desired angle noted above. The purpose of the flat section on the load applicator was to prevent lift off of the combined loading platen from the posterior rim of the vertebral body.

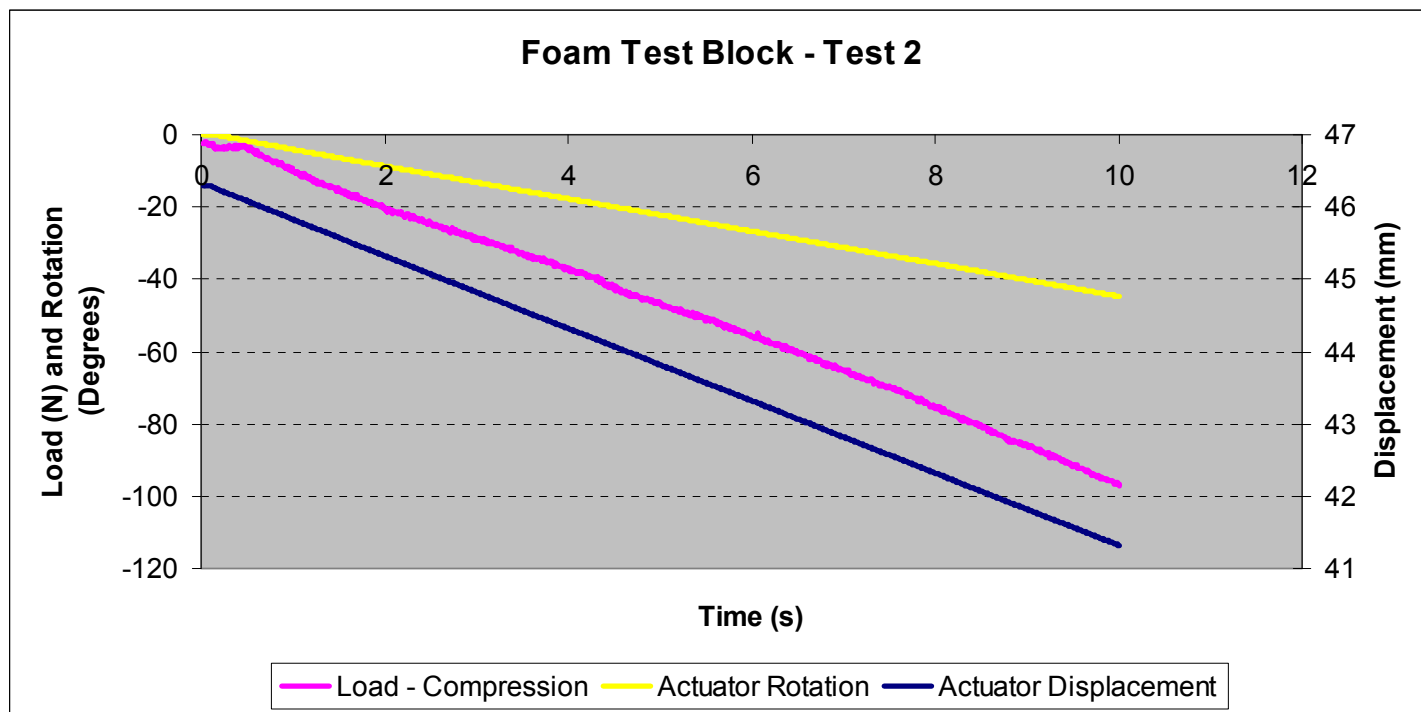


Figure 9: Prototype test #2. Foam block spinal surrogate.

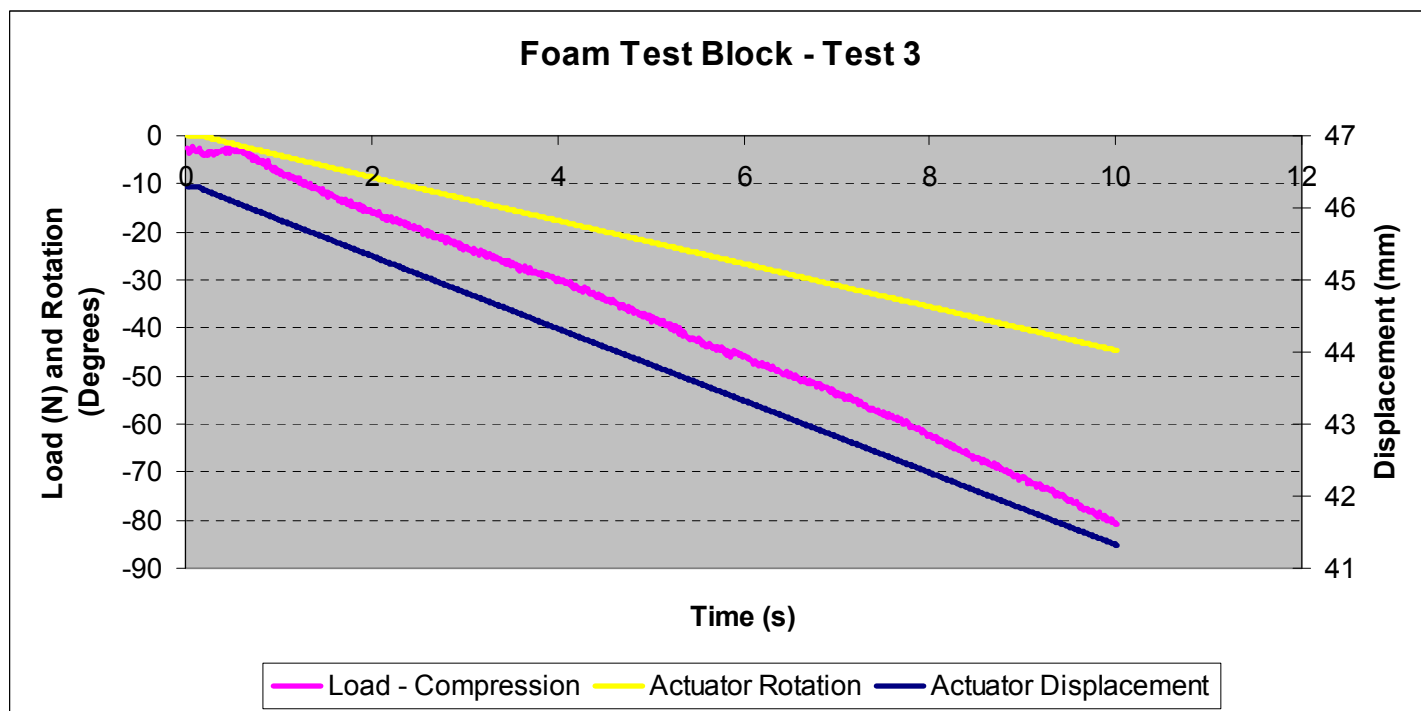


Figure 10: Prototype test #32. Foam block spinal surrogate.

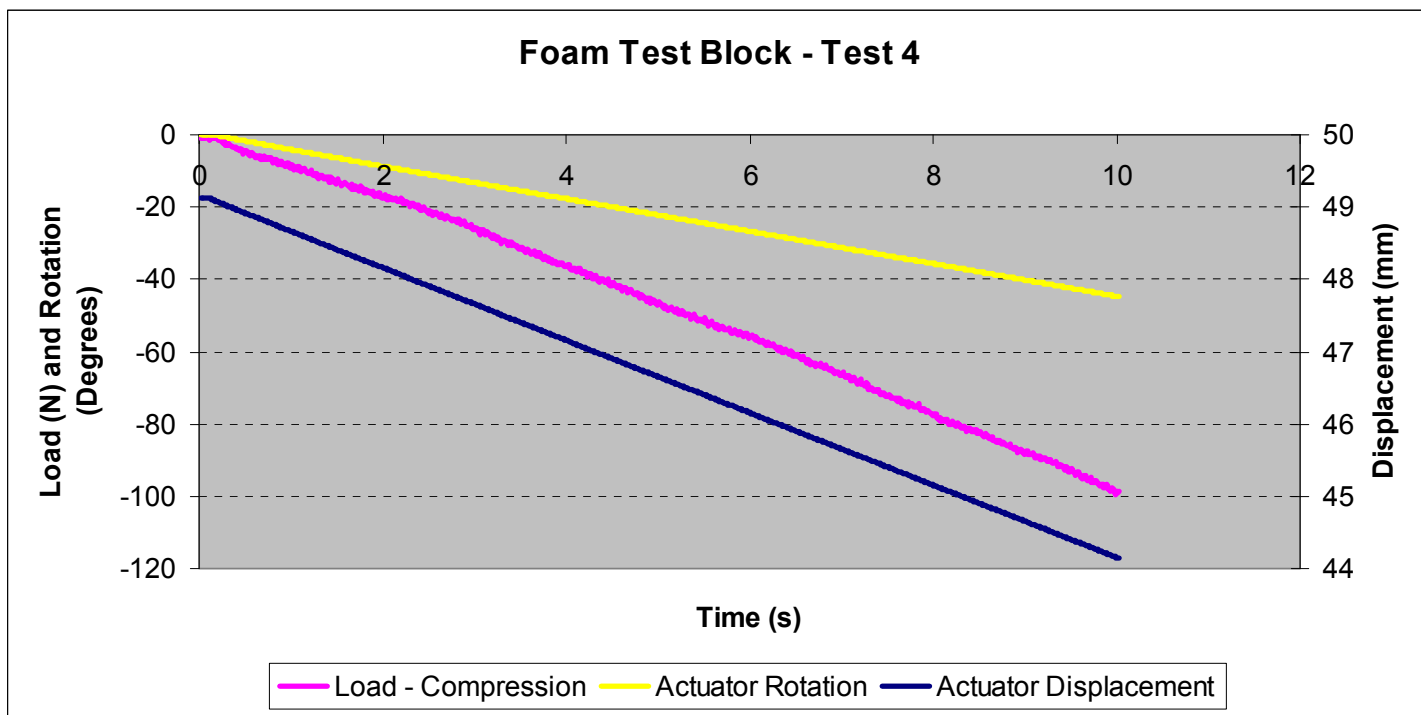


Figure 11: Prototype test #4. Foam block spinal surrogate.

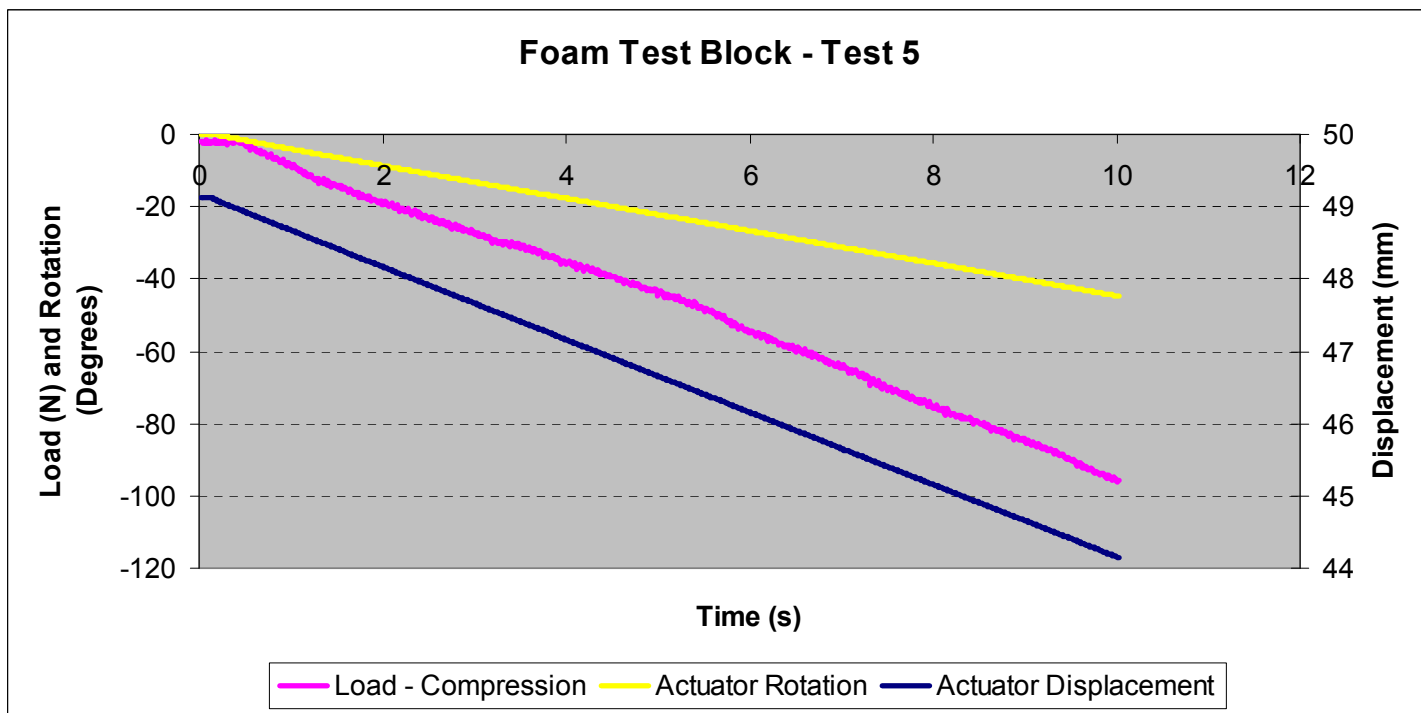


Figure 12: Prototype test #5. Foam block spinal surrogate.

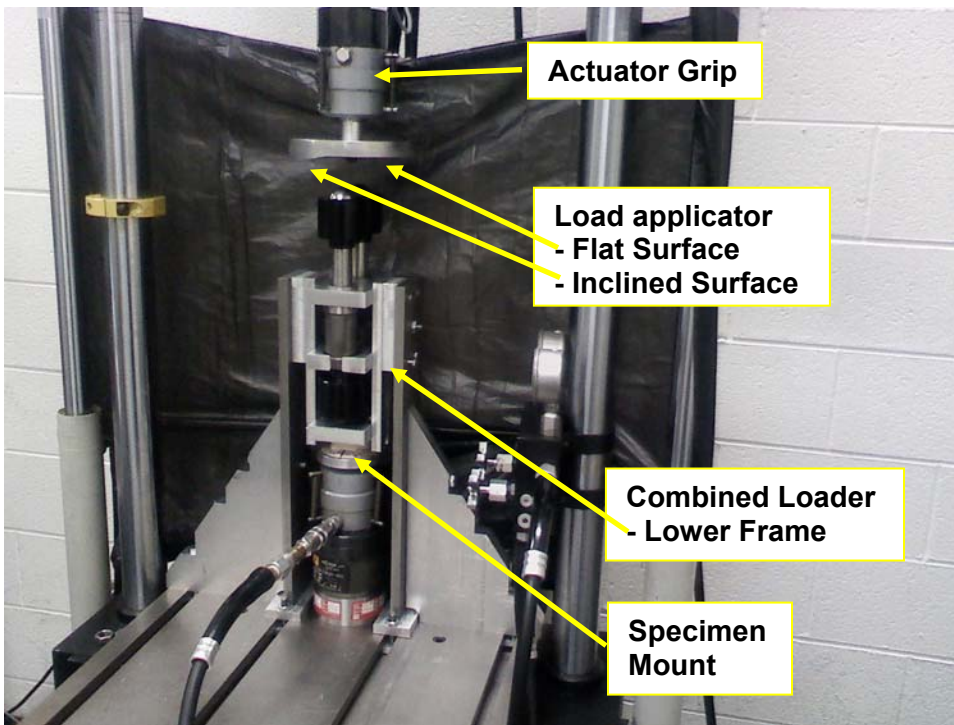


Figure 13: Combined Loading Fixture. Load applicator attached to the test machine actuator is shown with flat and inclined sections.

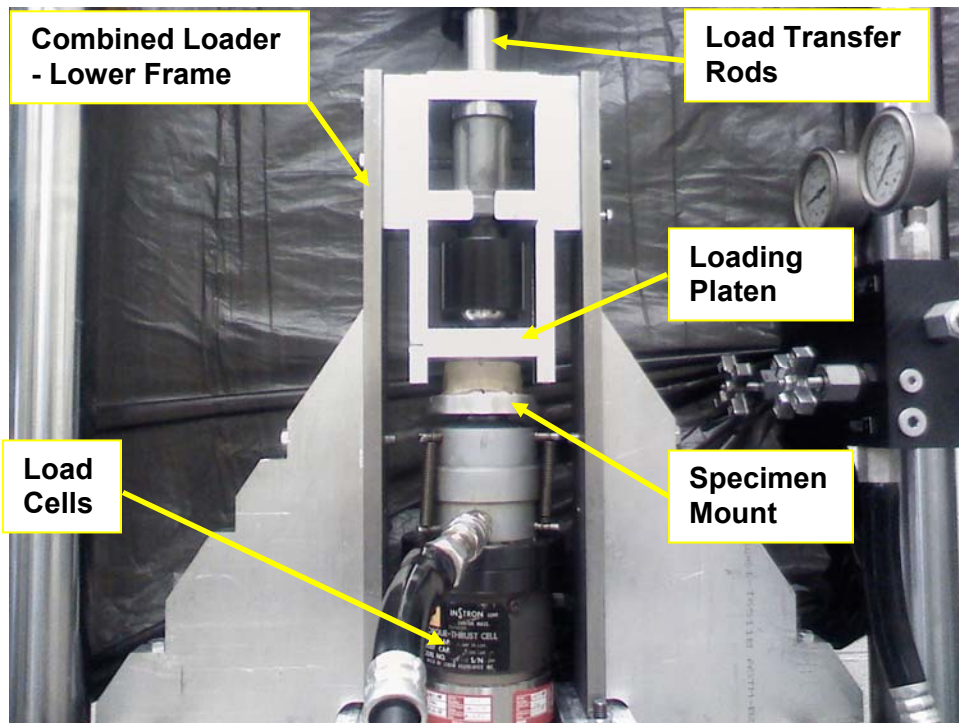


Figure 14: Combined Loading Fixture – Lower Frame. Lower Frame shows the load transfer rods, loading platen and specimen mounted and attached to load cell.

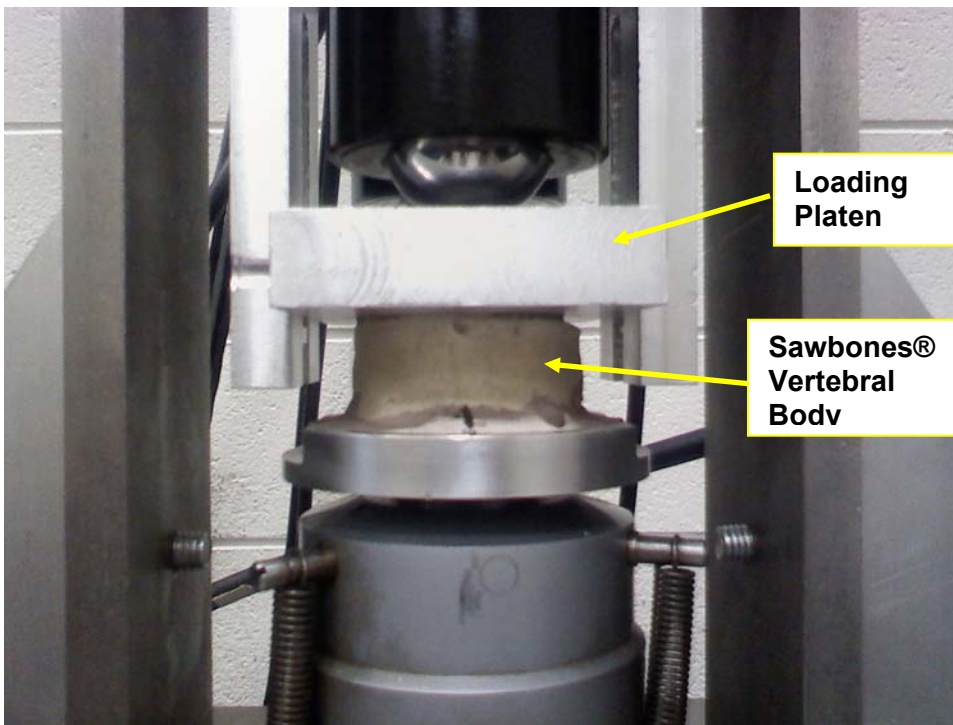


Figure 15: Combined Loading Fixture – Lower Frame, Loading Platen and Specimen Mount. Picture shows a Sawbones® surrogate vertebral body specimen positioned in the loading fixture between the loading platen and specimen mount. View is in the A-P direction and bending will be applied anteriorly in the sagittal plane.

In our calculations we have assumed that the vertebral body loading, with the combined loading fixture, will conform to a beam theory cantilever model (**Figure 16**). The model assumes a fixed end (the potted inferior vertebral endplate) and a guided opposite end (superior vertebral endplate). The input forces are P (compressive load) and W (transverse load), with W placed at a distance a from the superior endplate. In this case, a equals zero. The reaction moments at the superior and inferior endplates can be calculated from these loads. The forces (P & W) are directly measured with a 3-axis load cell (FUTEK Advanced Sensor Technology Inc., Irvine CA, USA).

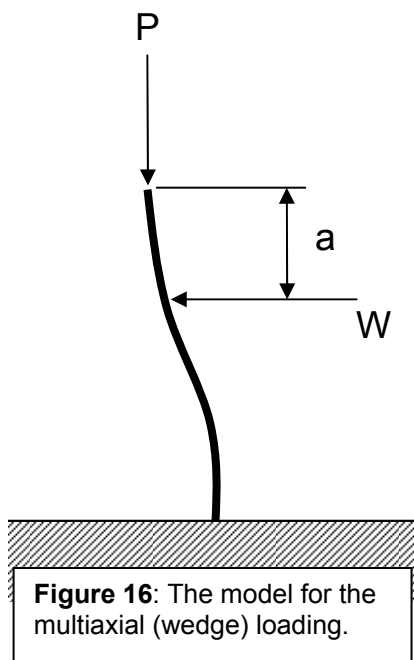


Figure 16: The model for the multiaxial (wedge) loading.

Multiple tests were conducted on a Sawbones® vertebral body using the combined loading fixture. Test modes included compression only, bending, and combined compression and bending. Compression and combined loading tests were conducted with an endpoint uniaxial displacement of 2mm and 1mm, respectively, in the vertical (z-axis) direction at a rate of 0.1 mm/s. Bending and combined loading tests were conducted with a rotary actuator endpoint rotation of 30°-40° and 20°-30°, respectively, at a rate of 1°/s. The observed loads were within the expected range of loads for cadaveric vertebrae. Loads ranged from 4993N to 9047N. During these tests it was noted that the z-axis displacement did not travel to the programmed endpoints or at the programmed displacement rate. The result was endpoint displacements that increasingly deviated from the programmed endpoint as the distance travelled increased (**Figure 17**). Also the displacement behavior at the transition between downward and upward travel became nonlinear. The first three displacement-time curves (1.0 mm endpoint – 1mm/s, 1.5 mm endpoint – 1mm/s, 2.0 mm endpoint – 1mm/s) show that the actual displacement was 83% and 77.0% of the programmed endpoint for 1.0 mm of travel and 2.0 mm of travel, respectively. The displacement rates had similar deviation from the programmed value. This issue was found to be a result of the PID gain settings of the displacement control feedback loop in the materials test machine. The PID gain settings were modified to optimum settings for the test setup, which corrected the endpoint displacement and rate to a maximum of 91% of the programmed values (1.0 mm endpoint – 0.1mm/s – P30I20), without the actuator control becoming unstable.

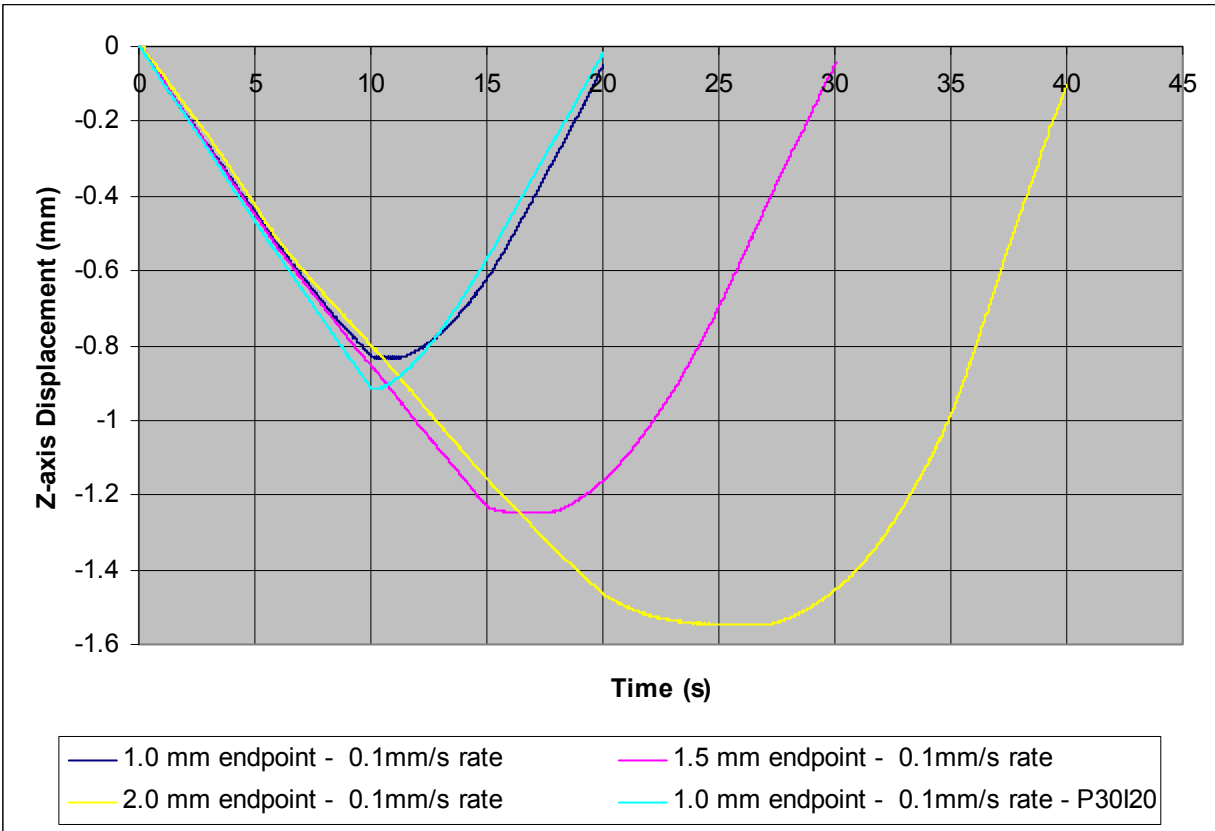


Figure 17: Comparison of z-axis displacement deviation from programmed endpoint and displacement rate. The deviation between the programmed and actual travel increases as a function of the endpoint distance.

Another aspect of the displacement deviation that has to be accounted for is the machine compliance. During a mechanical test, the recorded displacement of the actuator is comprised of specimen and test apparatus deformations (Kalidindi et al., 1997):

$$\delta_R = \delta_C + \delta_S \quad (1)$$

where, δ_R is the recorded displacement of the actuator, δ_C is the deformation of the test apparatus, the combined loading fixture in this case, and δ_S is the specimen deformation. Tests are currently being conducted to characterize the machine compliance by defining an expression for the test apparatus deformations in terms of the applied force $\delta_C(F)$. Once characterized, the test apparatus deformations can be computed from any mechanical test dataset (δ_R, F), using the previously defined expression $\delta_C(F)$. A corrected dataset of specimen deformations (δ_S, F) can then be computed by subtracting δ_C from δ_R to obtain δ_S . Accurate specimen deformation measurement is also being supplemented with the addition of two displacement measurement transducers to measure axial and transverse displacement of the specimen.

Testing, derivation of $\delta_C(F)$, and validation of the beam theory model is expected to be complete by the end of November 2012, at which point mechanical testing can proceed.

Task 6. Publications, Reports and Proposal Writing (Months 11-12)

Kim, W., Oravec, D., Sander, E., Divine, G. W., Flynn, M. J. and Yeni, Y. N., "Digital Tomosynthesis-Derived Microstructural Parameters Predict Cancellous Bone Stiffness in Human Vertebrae"
Conference abstract submitted to the 59th Annual Meeting, Orthopaedic Research Society, January 26-29, 2013, San Antonio, Texas.

Kim, W., Nekkanty, S., Oravec, D., Sander, E., Divine, G. W., Flynn, M. J. and Yeni, Y. N., "Digital tomosynthesis as a potential vertebral fracture risk assessment tool"
Manuscript in preparation to be submitted to Spine. A first draft is generated, under revision by the first author.

We are in the process of requesting a no-cost extension. This annual report meets the aim of writing a report.

Results:

Results from Task 2

Density Phantom Images

If the analysis region is limited to the central portion of the cylinder, a nonlinear relationship was found between radiographic density (DTS gray values) and solution density (**Figure 18a, b**) (A cubic polynomial explains over 99.9% of this relationship). The within-session and between session variability of density phantoms was less than 5% (coefficient of variation=0.5% to 4.7%) with largest variations caused by air (3.5% and 4.7% for within- and between-session variability, respectively).

Radiograph gray value was found to have a linear response to increased solution density (**Figure 19**).

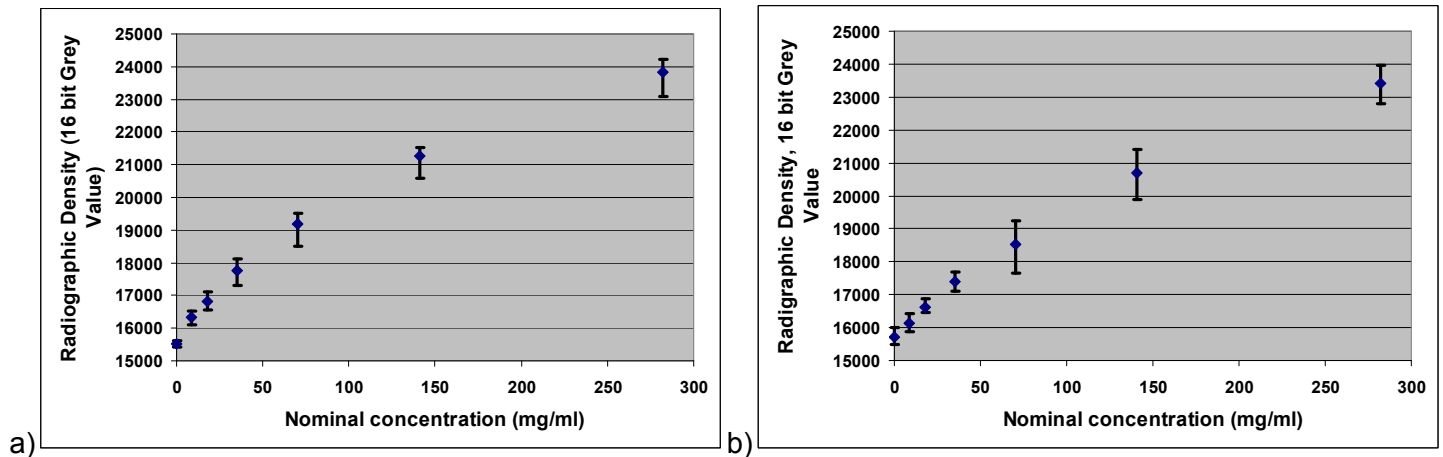


Figure 18: a) Average DTS gray value versus solution density for 5 sessions. b) Average DTS gray value versus solution density within a single session. Error bars represent between-session gray value range.

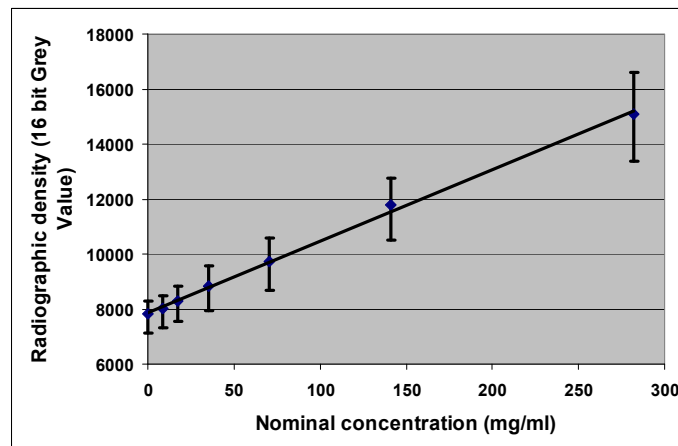


Figure 19: Average DTS gray value versus solution density vs solution concentration obtained from DTS radiogram. Error bars represent the range of gray values. ($R^2=0.9981$ for linear regression.)

Although the nonlinear relationship found between gray values and density in DTS images may be useful for quantitative purposes, the edge enhancement apparent in DTS images may affect neighboring radiographic density values making quantitative density measurements difficult. On the other hand, the high resolution digital radiography capabilities of the DTS system offer another possibility for density measurements (Kinds et al., 2011). Combined with the structural analyses from the DTS images, density measurements from the DTS radiograms may result in a powerful tool for bone quality assessment.

Spacing phantoms

Visual Analysis of DTS Spacing Phantom Images

The 350 and 300 μm spacing phantoms could be resolved visually when oriented 0° , 22.5° , and 67.5° to the

scanning direction. The 250 and 200 μm phantoms could only be partially resolved, while 150 and 100 μm phantoms had minimal texture and no visually detectable banding pattern. At the 90° orientation, textural information was completely lost for all spacing phantoms.

Quantitative Analysis of Microcomputed Tomography and DTS Spacing Phantom Images

Average FFT-measured layer thickness agreed well with thicknesses measured by micrometer during phantom preparation, supporting the use of micro-CT images as an established reference for further analyses.

For DTS images, of the four phantom angles relative to the scanning direction, orienting the length of the spacing phantom in line with the scanning direction yielded the greatest magnitude of frequency (0° off scanning direction in **Figure 20a**). Taking the 0° angle as a best resolution case, the FFT analysis method on DTS images accurately identified the phantom spacing for 350 μm and 300 μm , but the peaks were lost at narrower spacing (higher frequencies) consistent with the Nyquist criterion (**Figure 20b**).

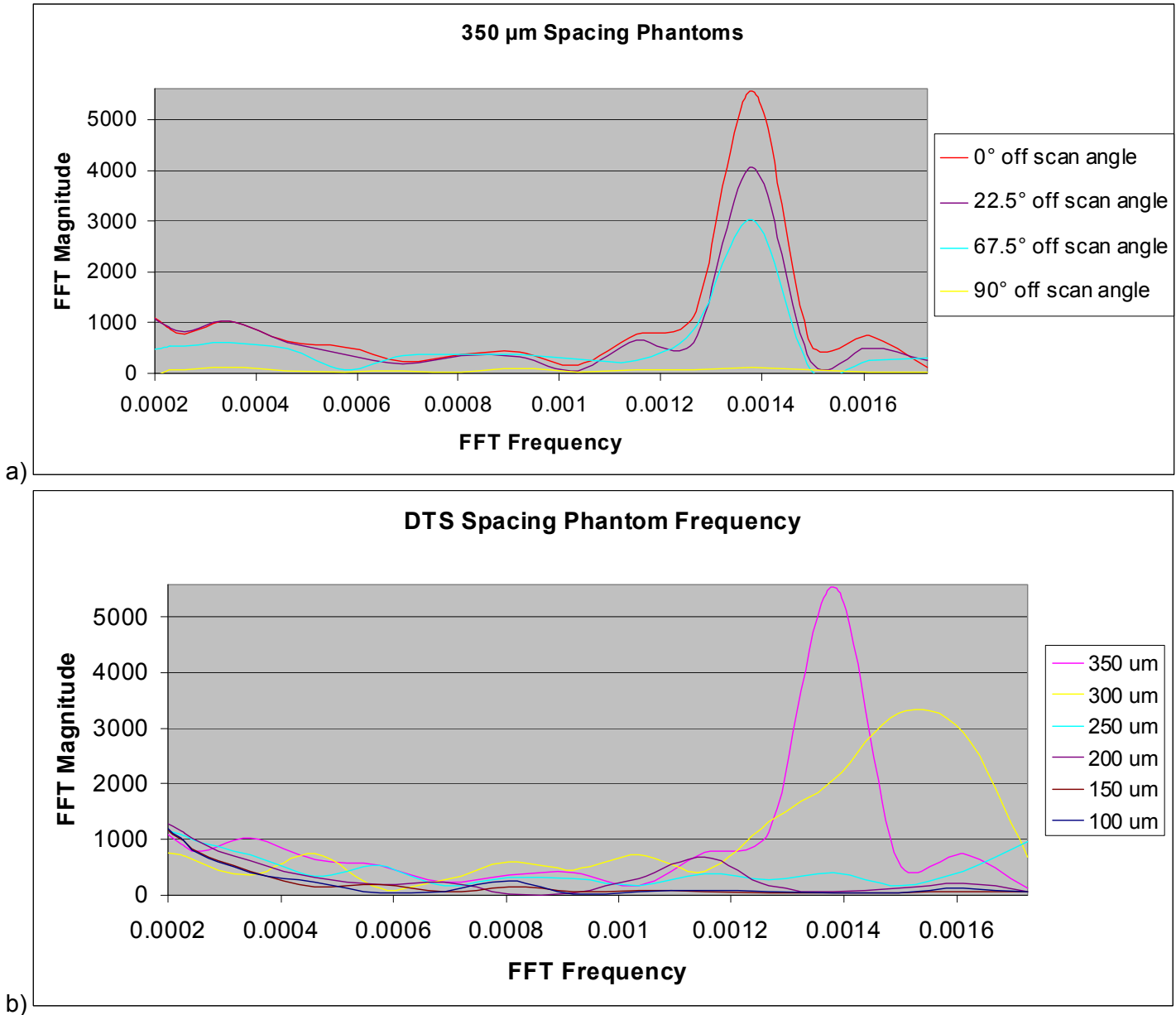


Figure 20: a) FFT magnitude was highest when layers of spacing phantom were oriented perpendicular to the scanning direction. **b)** For the 0° angle scan, the FFT method was able to identify spacing accurately for 350 and 300 μm spacing phantoms, but 250 μm and below could not be resolved.

In the MIL, LFD and fractal analyses, we interpret the results with the goal of finding parameters that are sensitive to changes in spacing, i.e., those that monotonically increase or decrease with increasing spacing and those that correlate with micro-CT measurements of the same kind.

Most of the MIL and LFD parameters measured from DTS did not follow a monotonic relationship with spacing for the full range of spacing, although some trends could be visible (**Figure 21a, b**). LFD parameters generally performed better than MIL parameters. Consequently, higher correlations were found between DTS LFD and micro-CT LFD parameters than between DTS MIL and micro-CT MIL parameters ($R^2=0.60$ for MIL.SD vs $R^2=0.64-0.95$ for LFD.Max, LFD.EllipseMax, LFD.DA, and LFD.SD). Especially noteworthy is the anisotropy of LFD for which DTS and micro-CT correlated 95%.

Fractal dimension decreases with phantom spacing (increasing image homogeneity) until 150 μm , below which aluminum is inseparable from plastic to resolve a scale-dependent pattern (**Figure 21c**). The decrease in lacunarity following a peak at 250 μm is possibly because texture heterogeneity is no longer detected due to low resolution and the image appears uniform to the lacunarity analysis (**Figure 21c**).

Thickness Phantoms

Visual Analysis of DTS Thickness Phantom Images

Aluminum thicknesses of 120, 115, 90, 75, and 60 μm phantoms could be resolved visually when oriented 0°, 22.5°, and 67.5° to the scanning direction, while 25 μm phantoms had minimal texture and no visually detectable banding pattern. At the 90° orientation, a banding pattern could be identified visually in 120, 115, 90, and 75 μm phantoms, but not in 60 and 25 μm phantoms.

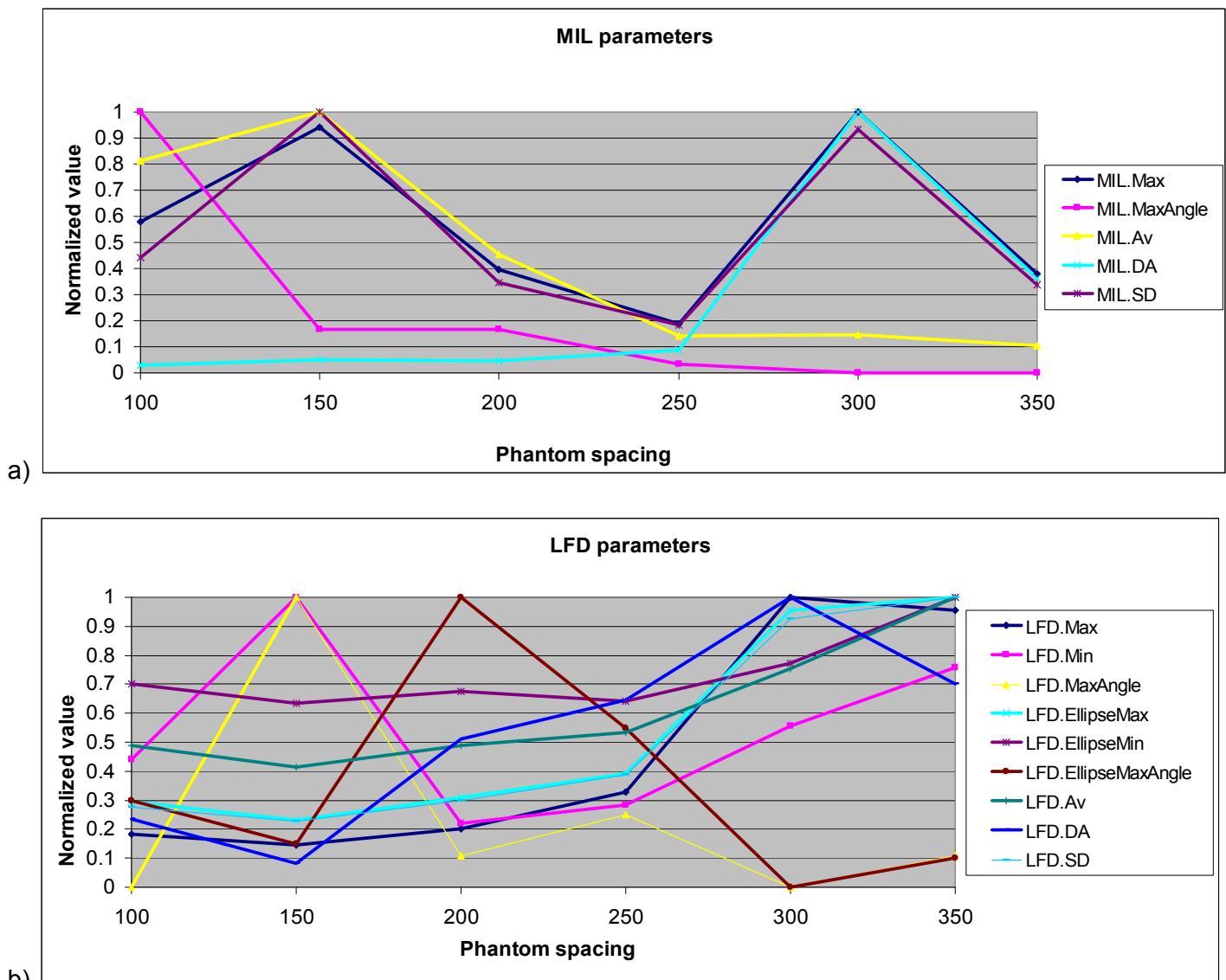


Figure 21

Figure 21 continued

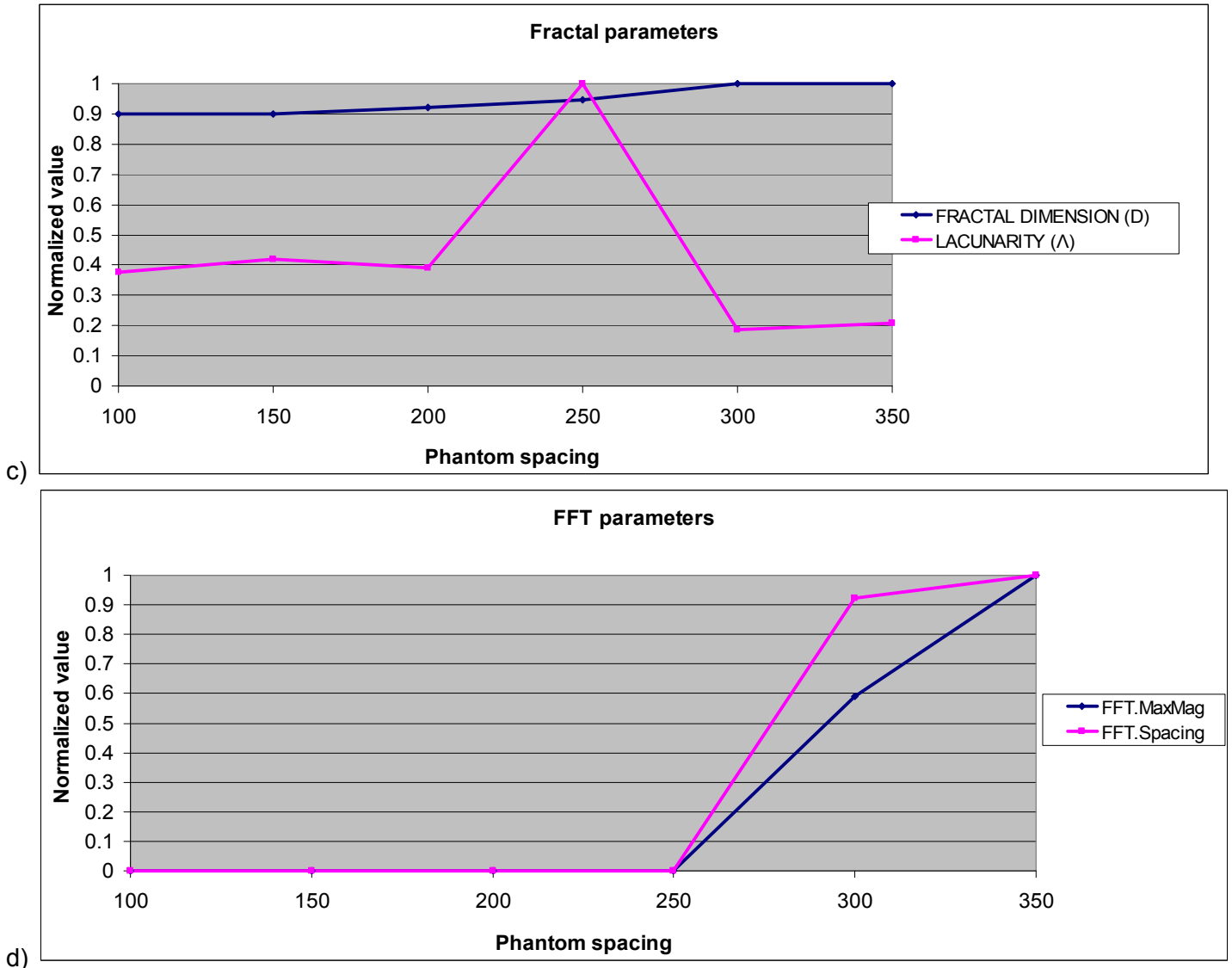


Figure 21: The changes in morphometric parameters with varying phantom spacing as measured from DTS images. All parameters are normalized for comparison purposes. a) MIL, b) LFD, c) fractal and d) FFT parameters.

As with the spacing phantoms, thicknesses were resolved best in the 0° scan, well in the oblique angles, and worst in the 90° scan. This is demonstrated as a weakened response of FFT magnitude at the same frequency at different specimen orientations (**Figure 22a**). FFT magnitude decreased together with decreasing layer thickness until 75 μm , below which aluminum could not be resolved from plastic by the analysis method. Taken together with spacing phantom results, FFT appears to be a sensitive tool for determining presence of small, sufficiently separated features within a structure. The effect of angle on resolving power emphasizes the importance of performing serial scans at various angles to extract the maximum amount of available structural information.

Although FFT analysis was able to resolve frequencies down to 75 μm , a banding pattern was still visible in the 60 and 25 μm phantoms, albeit faint. For this reason, MIL, LFD, and fractal analyses were again performed on regions cropped from micro-CT and DTS images. MIL.Max, MIL.DA, and MIL.SD decreased with plate thickness (**Figure 23a**). Of the aforementioned MIL parameters, MIL.Max and MIL.SD were moderately correlated to micro-CT MIL measurements ($R^2=0.68$ and 0.72 , respectively). Among the LFD parameters, LFD.Max, LFD.SD, and LFD.EllipseMax decreased monotonically with thickness down to 25 μm . Of these LFD parameters, LFD.Max, LFD.Av, LFD.SD, and LFD.EllipseMax were highly correlated with micro-CT LFD measurements ($R^2=0.97$, 0.97 , 0.95 , and 0.98 , respectively). Fractal dimension remained relatively constant while lacunarity decreased monotonically with thickness down to 25 μm . These findings suggest MIL, LFD and fractal analyses can detect changes in feature thickness. However these changes in the measured parameters

are of correlational nature with respect to the underlying structural changes at small resolutions.

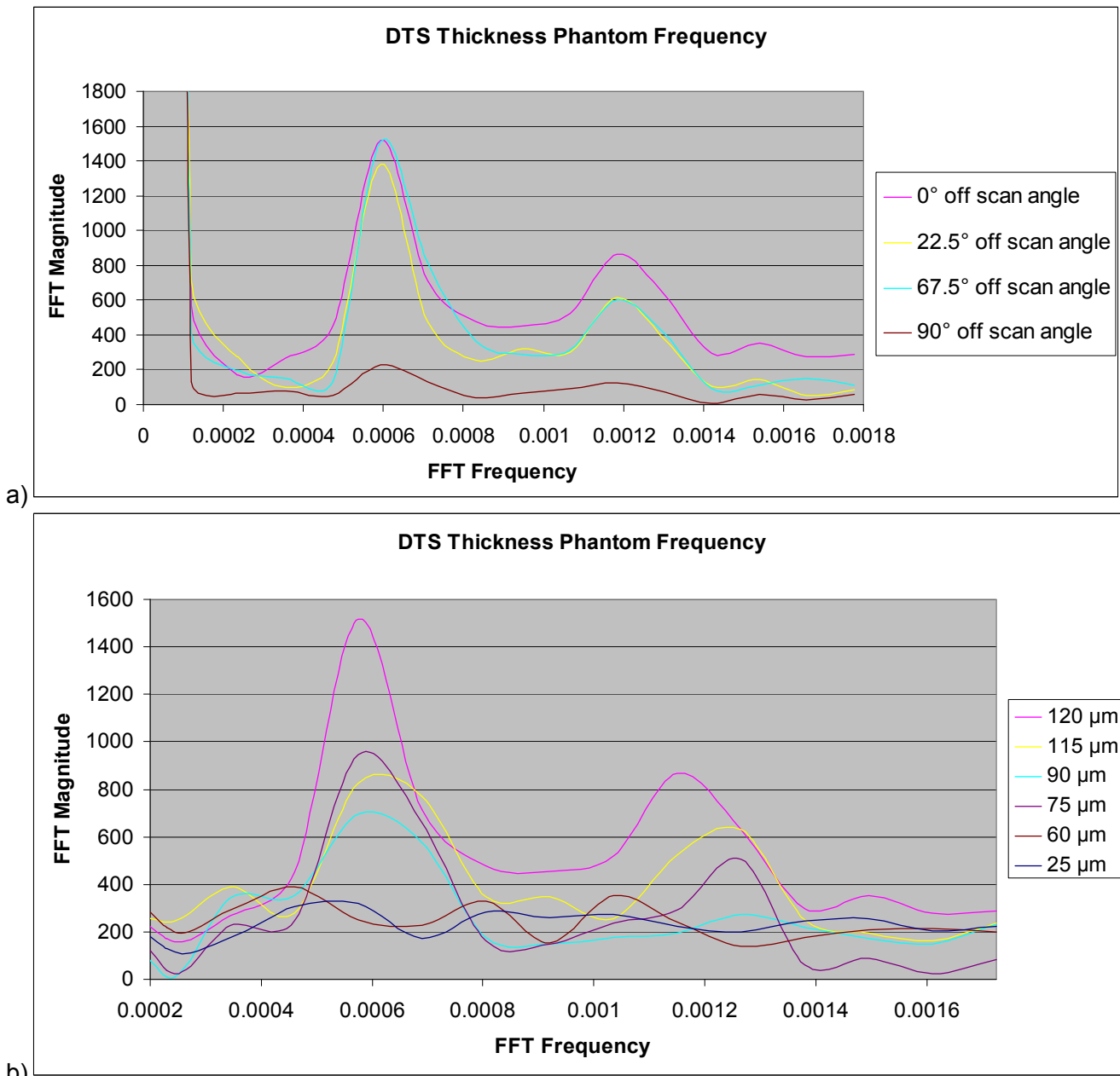


Figure 22: a) FFT magnitude was highest when layers of thickness phantom were oriented perpendicular to the scanning direction and lower when layers were parallel. **b)** For the 0° angle scan, the FFT method was able to identify thickness accurately for 75-120 μm thickness phantoms, but 60 μm and below could not be resolved.

Aluminum grid panel phantom

All DTS images exhibited a varying degree of “halo” artifacts adjacent to the aluminum grid (**Figure 24a, b**). The gray value of the aluminum grid was shown as a valley as it exhibited a higher attenuation due to its higher density than air (**Figure 24c**). The location of this valley was used to determine the location of the grid and the amplitude was used to monitor signal variations in the DTS images.

All gray value profiles generated from L1 and L2 measurements of 11 slices /stack in four orientations (0°, 15°, 22.5° and 45°) are plotted in **Figure 25**. Within each plot box in **Figure 25**, the 11 gray value distributions within each image slice stack overlap nearly perfectly along the x-axis (transverse distance from the center of image). These results indicate that along between 0 mm to 11 mm (i.e. z-axis = depth of grid panel), there is no significant sliding of peak locations in both L1 and L2 measurements. Furthermore the results revealed that, while most of the plot boxes show clear signals of peaks (gray value range: 100-20), signals at 0° L2 orientation performed poorly. This confirms results from spacing and thickness phantoms at the 90° (parallel)

angle, indicating that DTS performs poorly in reconstructing structural features that are parallel to the scanning direction (also (Flynn et al., 2007)).

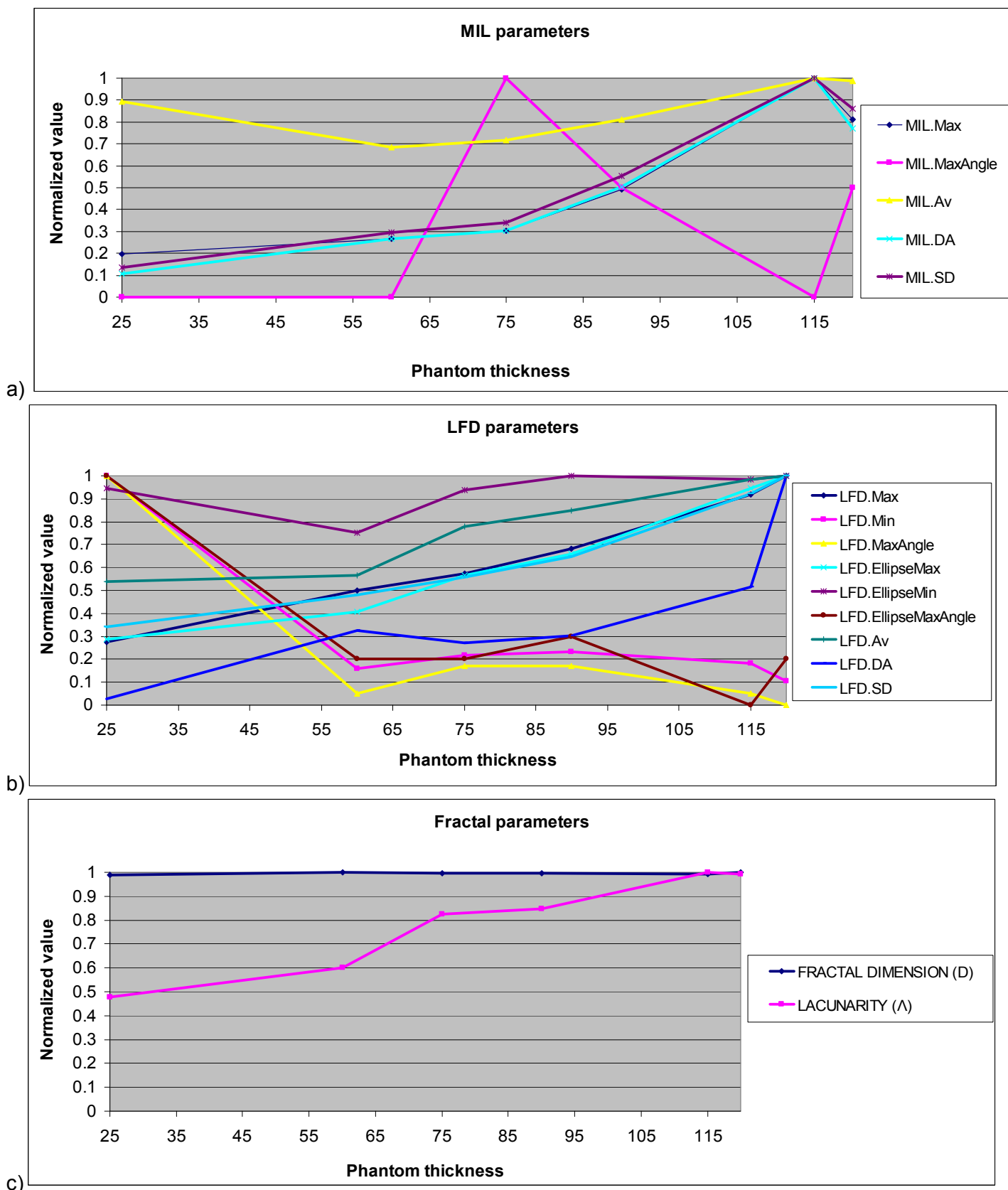


Figure 23

Figure 23 continued

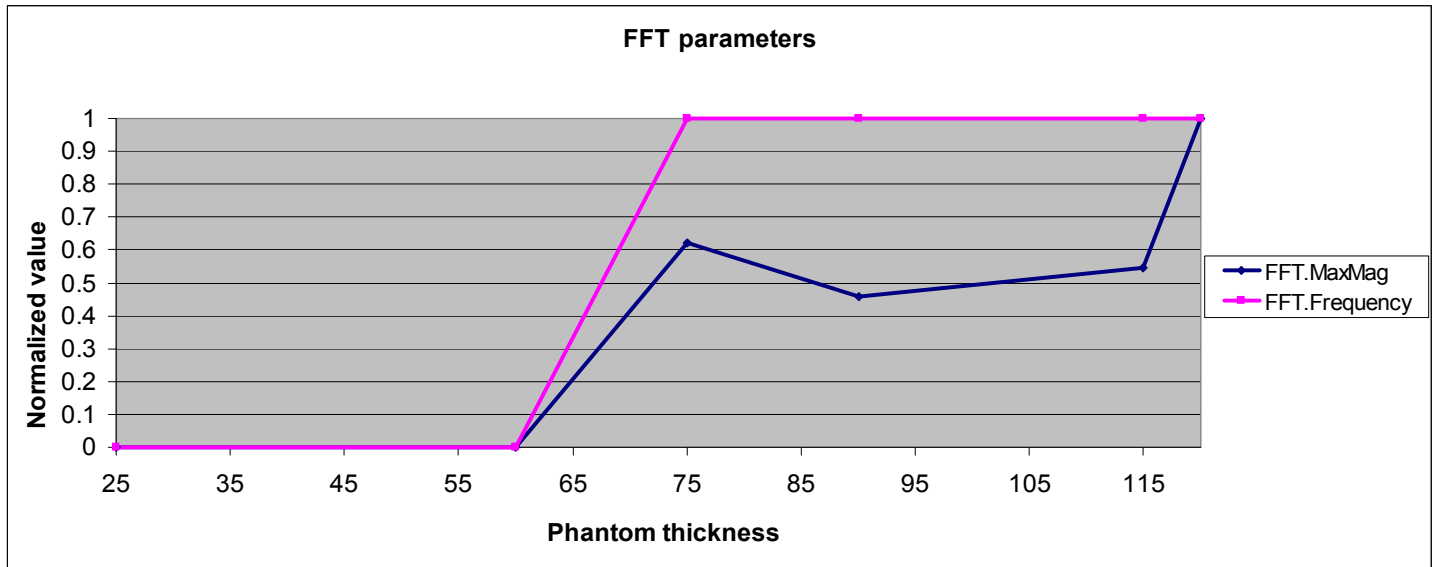


Figure 23: The changes in morphometric parameters with varying phantom thickness as measured from DTS images. All parameters are normalized for comparison purposes. a) MIL, b) LFD, c) fractal and d) FFT parameters.

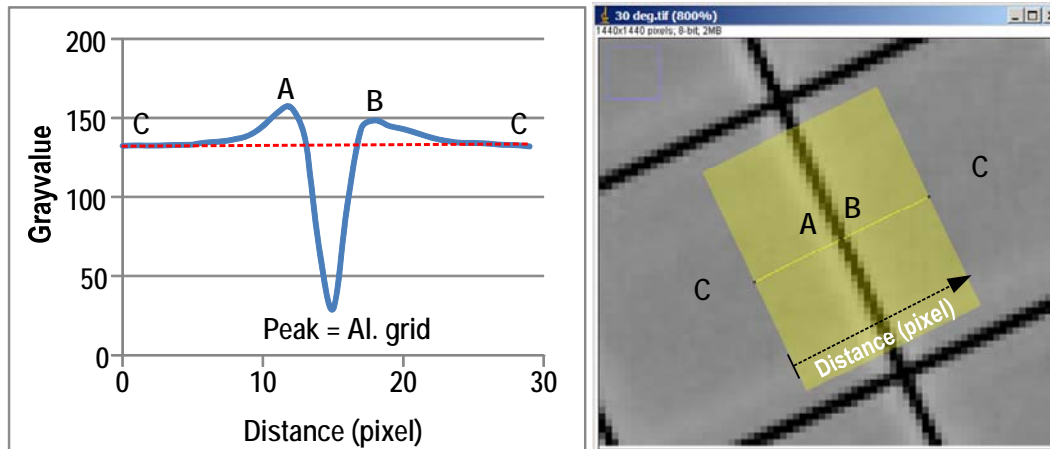


Figure 24: A typical gray value profile distribution in the ROI shown in yellow. The DTS image has a characteristic “halo” (A and B) reflecting a sudden change in density (i.e. air-to-aluminum). The halo has a slightly higher gray value (i.e. whiter). The air is marked as C.

Table 1 shows the mean and standard deviations of peak interval distances within each ROI. The table also confirms that there is a minimal variation of mean interval distance between grids within each ROI setting as well as among the eight orientations. The results indicate that there is no measurable distortion effect among two different measurement orientations (L1 vs. L2) as well as different scanning orientations (0°, 15°, 22.5° and 45°). This in turn assures that the dimension data obtained in DTS is likely to be reliable given that the subject geometry, structure and density characteristics are comparable to the aluminum grid used here.

Table 1: Mean and standard deviations of peak interval distances of different ROIs.

Orientation-ROI	0° L1	0° L2	15° L1	15° L2	22.5° L1	22.5° L2	45° L1	45° L2
No. grids in ROI (n)	20	17	19	17	17	17	18	16
Mean interval distance between two peaks (mm)	12.5	12.6	12.6	12.6	12.6	12.6	12.6	12.6
Standard deviation	0.14	0.14	0.14	0.14	0.14	0.14	0.14	0.14

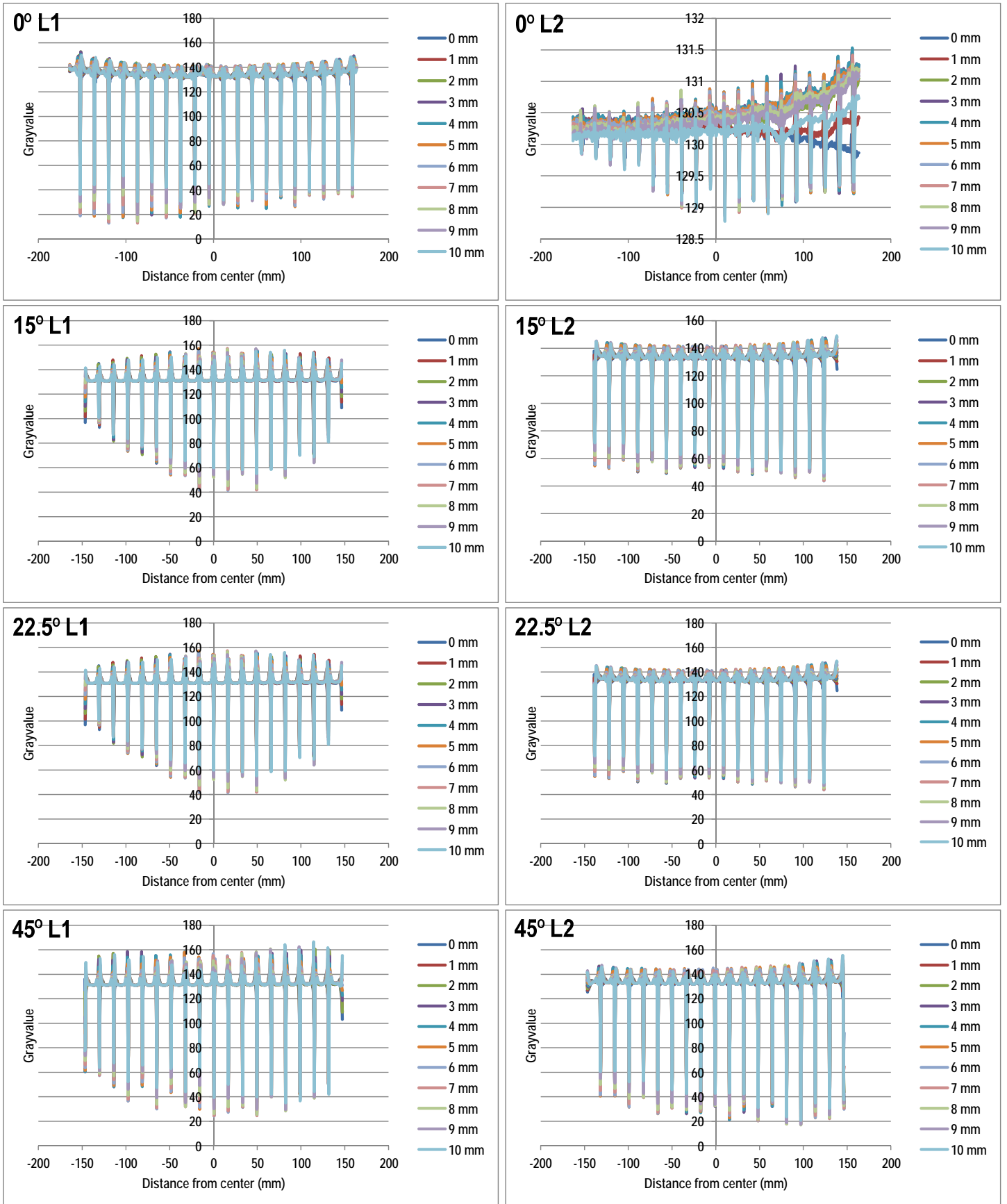


Figure 25: Gray value profile plots of L1 and L2 ROIs from 0°, 15°, 22.5° and 45° scanning orientation. Note how all peak locations are near perfectly aligned between different slices within each ROI.

Mean peak values of 11 slices from each angular orientation ($n = 8$) were plotted in **Figure 26**. In general, the data indicate that the level of signal strength (gray value) is affected by i) angular orientation of the grid relative to the scan direction, ii) angle of measurements (L1 vs L2) within each scanning orientation and iii) distance

from the center of the scanning area.

While 0° L1 and 45° L1 generated highest signal levels, the signal from their L2 counterparts was much less; 0° L2 generated nearly no signal and 45° L2 generated approximately 40% less signal than that of 45° L1. The differences between L1 and L2 were reduced in 15° and 22.5° sets, however overall, as a set L1 and L2 at 22.5° performed best. The near-zero signal of 0° L2 confirms the previous observation that features that are parallel to the direction of tomographic acquisition are not well resolved in the final DTS image (also (Flynn et al., 2007)).

The signals varied as the distance from the center of the detector panel varied, for example from the left (-ve) to right (+ve), the signals of 45° L1, L2 and 22.5° L1 increased, 0° L1 decreased and 15° L2, 22.5° L2 formed a plateau at the center and their signals decreased at the edges of measurement area. In general scans performed in oblique orientations resulted in more uniform signals across the ROI.

Based on the results of the grid study, it is recommended that additional scans performed at 22.5° orientation should be explored for objects that contain both vertical and horizontal features such as vertebral bodies. Furthermore the finding that signal levels in the 22.5° scanning orientation are relatively uniform across the measuring area of 30 x 30 cm ($\pm 150\text{mm}$ as shown in **Figure 26**) supports this approach as this ROI is large enough to image six to eight levels of spine at once.

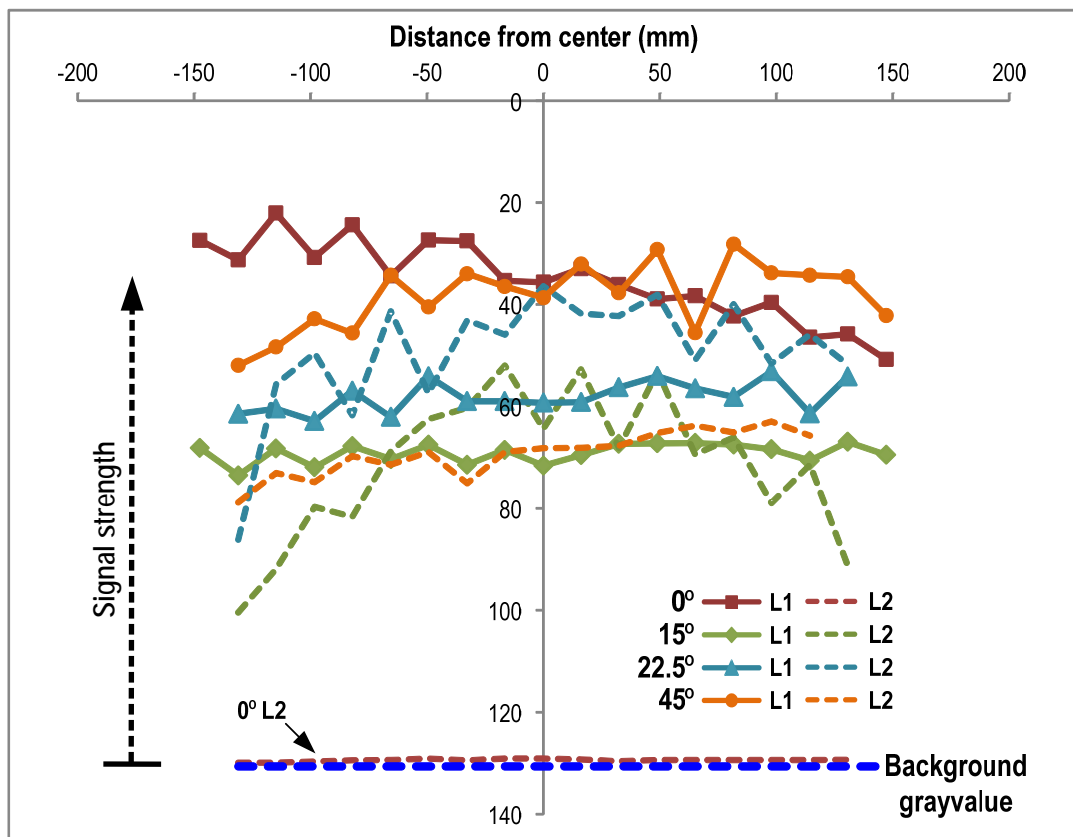


Figure 26: Mean peak gray value profiles of all ROI orientations. The plots are drawn upside down to show signal strength relative to the background signal (= ~130 in blue).

Results from Tasks 3 and 4

Statistical analysis was carried out in two parts using JMP 10 (Cary, NC). The first part aimed at examining the relationships between micro-CT-derived and DTS-derived parameters of cancellous microstructure. The analysis consisted of mixed linear regression models between stereological parameters of μCT (BV/TV, Tb.Th, Tb.N, Tb.Sp, DA) to DTS parameters (fractal, MIL and LFD). Mixed models were used in lieu of simple regression models to account for pseudoreplication in the data. The second part of the analysis aimed at examining the ability of DTS-derived parameters to predict bone stiffness and stress distribution properties (E_{FEM} , VMCV and $\text{VMExp}/\sigma_{\text{app}}$), with and without BV/TV.Av in the regression equations. BV/TV.Av was introduced to the regression models to examine predication capability of DTS parameters beyond that of BV/TV.Av alone, in which BV/TV.Av was treated as a surrogate measurement of bone mass (i.e., clinical BMD). Statistical significance was set at $p <$

0.05. The multiple regression models were performed in a stepwise manner by eliminating parameters that exhibit multi-collinearity from the initial predictor set based on variance inflation factors ($VIF > 5$) and then eliminating parameters with nonsignificant effects ($p > 0.05$).

Table 2: Correlation coefficients (R) from mixed linear models where one μ CT parameter (columns) is the outcome and one DTS parameter (rows) is the effect variable. This table was constructed using mixed models instead of using simple correlations to account for pseudoreplication. Polarity of the correlation coefficient (\uparrow for positive and \downarrow for negative relationships) and the p-value (in round brackets) are given in each cell along with the R value. Only those models with $p < 0.05$ are shown.

	\uparrow/\downarrow R (p-value)	BV/TV.Av	Tb.Th.Av	Tb.N.Av	BV/TV.SD	Tb.Th.SD	Tb.N.SD	DA
Fractal Analysis	FD	\downarrow 0.88 (0.045)	\downarrow 0.69 (0.003)			\downarrow 0.66 (0.009)		
	S_{λ}	\downarrow 0.90 (0.001)	\downarrow 0.78 (<0.001)		\downarrow 0.82 (0.001)	\downarrow 0.78 (<0.001)		
Unsharp mask (USM)	MIL.Max				\downarrow 0.74 0.015		\downarrow 0.74 0.004	
	MIL.DA		\uparrow 0.67 0.010			\uparrow 0.76 <0.001	\downarrow 0.73 0.014	\uparrow 0.56 0.025
	MIL.SD		\uparrow 0.69 0.006			\uparrow 0.75 <0.001	\downarrow 0.74 0.007	\uparrow 0.54 0.048
	LFD.Max		\uparrow 0.60 0.036					
	LFD.Av		\uparrow 0.60 0.021				\uparrow 0.65 0.032	
Conservative binarization (Bin.Csv)	MIL.Max		\uparrow 0.72 (0.001)	\downarrow 0.92 (0.026)		\uparrow 0.77 <0.001	\downarrow 0.71 0.012	
	MIL.DA		\uparrow 0.72 <0.001			\uparrow 0.79 <0.001	\downarrow 0.74 0.015	\uparrow 0.57 0.018
	MIL.SD		\uparrow 0.74 <0.001			\uparrow 0.80 <0.001	\uparrow 0.73 0.012	\uparrow 0.55 0.030
	LFD.Max	\uparrow 0.90 0.012	\uparrow 0.77 <0.001			\uparrow 0.76 <0.001		
	LFD.DA		\uparrow 0.65 0.039			\uparrow 0.67 0.004		
	LFD.Av	\uparrow 0.89 0.0136	\uparrow 0.71 <0.001			\uparrow 0.71 0.002		
	LFD.SD	\uparrow 0.89 0.024	\uparrow 0.77 <0.001			\uparrow 0.79 <0.001		
Aggressive binarization (Bin.Ag)	MIL.Av			\uparrow 0.93 (0.031)				
	MIL.SD				\downarrow 0.78 (0.012)			\uparrow 0.54 (0.036)
	LFD.Max	\uparrow 0.89 (0.026)	\uparrow 0.67 (0.002)					
	LFD.DA							\uparrow 0.54 (0.029)
	LFD.Av	\uparrow 0.89 (0.012)	\uparrow 0.69 (0.001)		\uparrow 0.77 (0.043)	\uparrow 0.70 (0.003)		
	LFD.SD		\uparrow 0.59 (0.034)					

MIL and LFD parameters calculated from the conservatively binarized (Bin.Csv) images had stronger and larger number of significant relationships with micro-CT parameters than those from the unsharpened (USM)

and aggressively binarized (Bin.Ag) methods (**Table 2**). However, BV/TV.SD was not related to any DTS parameter from the Bin.Csv method. Fractal dimension and lacunarity slope parameters from fractal analysis also had strong relationships with micro-CT parameters. However, mean lacunarity was not related to the μ CT parameters. Interestingly, neither the magnitude nor the heterogeneity of Tb.Sp (Tb.Sp.Av and Tb.Sp.SD, respectively) was related to DTS parameters.

DTS images processed using the USM method provided parameters that were comparable to bone mass in their ability to explain E_{FEM} and $VMExp/\sigma_{app}$ but more explanatory than BV/TV alone for VMCV (**Table 3**). When used together with BV/TV.Av in multiregression models (simulating a situation where bone mass information is already available from another modality), addition of DTS-derived parameters contributed significantly to prediction of E_{FEM} and VMCV but not $VMExp/\sigma_{app}$. In addition to BV/TV, MIL.Max and LFD.Max significantly contributed to E_{FEM} and MIL.DA to VMCV. (**Figure 27**.)

Table 3: Summary of multi regression models of BV/TV-only, DTS-only and DTS+BV/TV for the predictions of E_{FEM} , VMCV, $VMExp/\sigma_{app}$ using unsharp mask method (USM). Only those with $p < 0.05$ are shown.

USM			DTS			μ CT	
Model	Components	R^2_{adj}	MIL.Max	MIL.DA	LFD.Max	BVTV.Av	Intercept
E_{FEM}	BV/TV	0.82				1695 ($<.001$)	-62.9 (0.057)
	DTS	0.84	-103 (0.004)		2833 ($<.001$)		313 (0.004)
	DTS+BV/TV	0.95	-47.7 (0.018)		1422 ($<.001$)	1833 ($<.001$)	-54.7 (0.423)
VMCV	BV/TV	0.59				-1.39 (0.005)	0.990 ($<.001$)
	DTS	0.82		-0.404 ($<.001$)	-1.52 (0.027)		1.39 ($<.001$)
	DTS+BV/TV	0.81		-0.385 ($<.001$)		-1.74 ($<.001$)	1.53 ($<.001$)
$VMExp/\sigma_{app}$	BV/TV	0.97				-50 ($<.001$)	14.7 ($<.001$)
	DTS	0.91	2.56 (0.003)		-43.7 (0.004)		1.59 (0.524)
	DTS+BV/TV	0.97				-50 ($<.001$)	14.7 ($<.001$)

Table 4: Summary of multi regression models of BV/TV-only, DTS-only and DTS+BV/TV for predictions of E_{FEM} , VMCV, $VMExp/\sigma_{app}$ using conservatively binarized method (Bin.Csv). Only those with $p < 0.05$ are shown.

Bin.Csv			DTS			μCT		
Model	Components	R ² _{adj}	MIL.DA	LFD.Max	LFD.Av	LFD.SD	BVTV.Av	Intercept
E _{FEM}	BV/TV	0.82					1695 (<.001)	-62.9 (0.057)
	DTS	0.82	102 (0.003)	-38.8 (<.001)				-38.8 (0.4374)
	DTS+BV/TV	0.94	-0.17 (0.034)	501 (0.035)			1952 (<.001)	-312 (<.001)
VMCV	BV/TV	0.59					-1.39 (0.005)	0.990 (<.001)
	DTS	0.86	-0.30 (<.001)			-8.12 (0.005)		1.19 (<.001)
	DTS+BV/TV	0.81	-0.30 (<.001)				-1.70 (<.001)	1.45 (<.001)
VMExp/σ _{app}	BV/TV	0.97					-50 (<.001)	14.7 (<.001)
	DTS	0.92			-96.3 (<.001)			-0.14 (0.975)
	DTS+BV/TV	0.97					-50 (<.001)	14.7 (<.001)

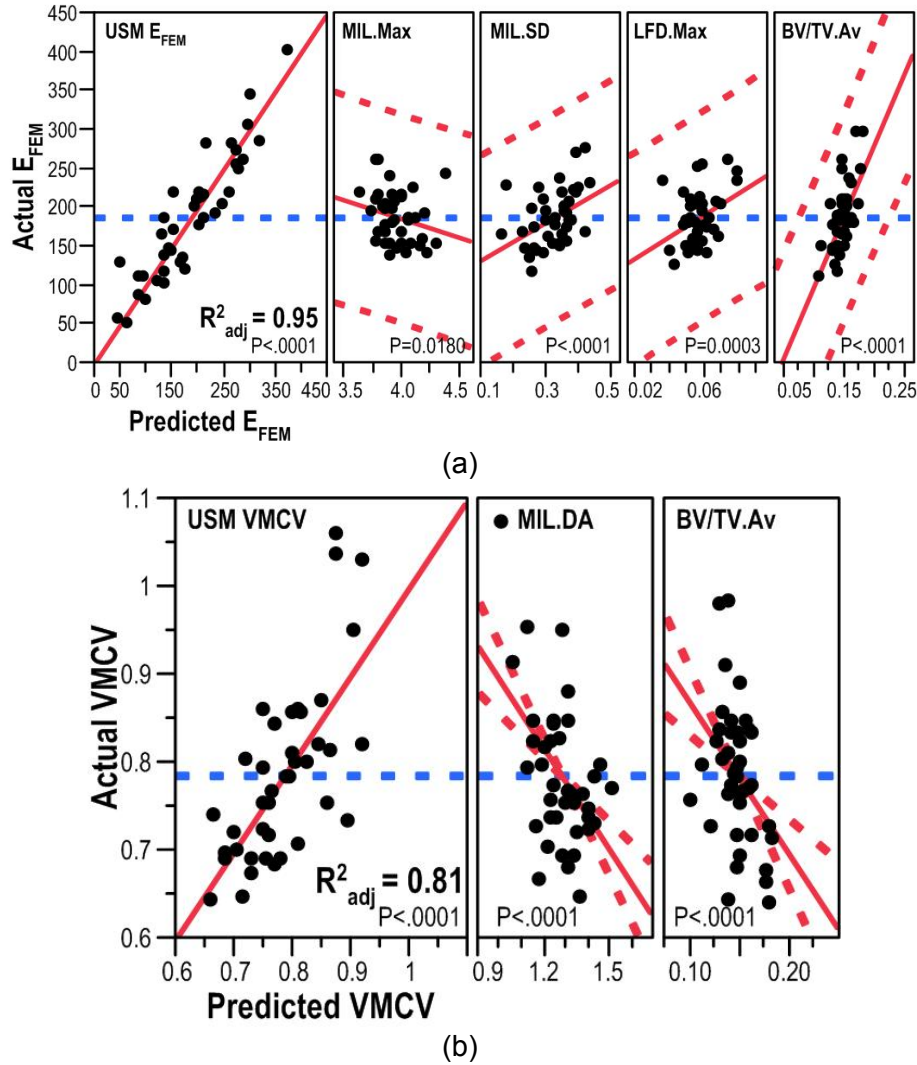


Figure 27: Multiple regression results from the unsharp mask (USM) processing method. Fit of the multiple regression models constructed using both BV/TV and DTS-based predictor variables and the leverage plots for the individual effects with the associated p-values for **a)** EFEM and **b)** VMCV. The blue and the red dashed lines show the mean of the response and confidence curves, respectively.

DTS images processed using the Bin.Csv method also provided parameters that were comparable to bone mass in their ability to explain E_{FEM} and $VMExp/\sigma_{ap}$ but more explanatory than BV/TV alone for VMCV (**Table 4**). When used together with BV/TV.Av in multiregression models (simulating a situation where bone mass information is already available from another modality), addition of DTS-derived parameters contributed significantly to prediction of E_{FEM} and VMCV but not $VMExp/\sigma_{app}$: In addition to BV/TV, MIL.DA and LFD.Max significantly contributed to E_{FEM} and MIL.DA to VMCV. (**Figure 28**.)

DTS images processed using the Bin.Ag method, similar to other methods above, provided parameters that were comparable to bone mass in their ability to explain E_{FEM} and $VMExp/\sigma_{ap}$ but more explanatory than BV/TV alone for VMCV (**Table 5**). When used together with BV/TV.Av in multiregression models (simulating a situation where bone mass information is already available from another modality), addition of DTS-derived parameters contributed significantly to prediction of E_{FEM} and VMCV but not $VMExp/\sigma_{app}$: In addition to BV/TV, MIL.DA and S_{λ} significantly contributed to E_{FEM} and, MIL.DA and LFD.Av to VMCV. In this case, there seems to be a confounding effect of BV/TV on most significant DTS parameters such that inclusion of BV/TV is worse than DTS alone. (**Figure 29**.)

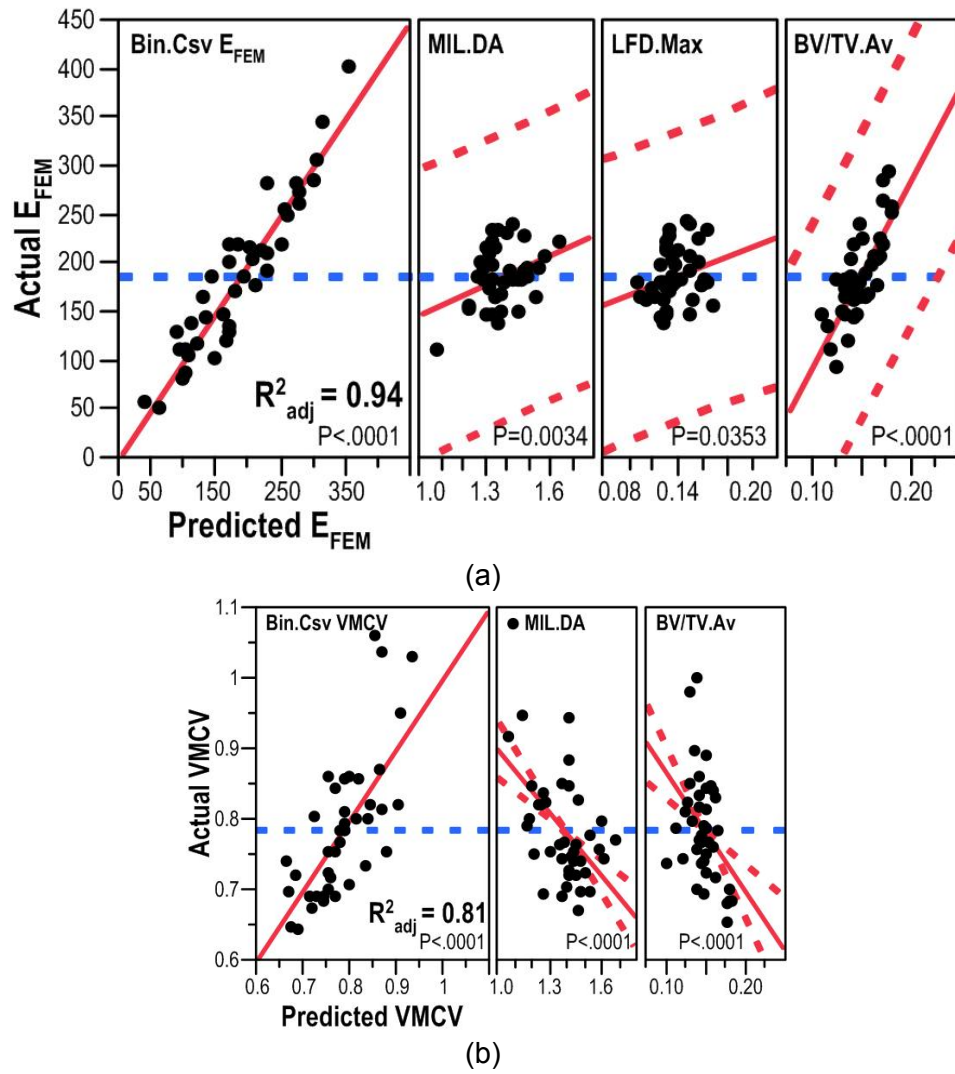


Figure 28: Multiple regression results from the conservatively binarized method (Bin.Csv). Fit of the multiple regression models constructed using both BV/TV and DTS-based predictor variables and the leverage plots for the individual effects with the associated p-values for **a)** EFEM and **b)** VMCV. The blue and the red dashed lines show the mean of the response and confidence curves, respectively.

Table 5 – Summary of multi regression models of BV/TV-only, DTS-only and DTS+BV/TV for predictions of E_{FEM} , VMCV, $VMExp/\sigma_{app}$ using aggressively binarized method (Bin.Ag). Only those with $p < 0.05$ are shown.

Bin.Ag		DTS		μCT						
Model	Components	R^2_{adj}	S_{λ}	MIL.Max	MIL.DA	MIL.Av	LFD.Av	LFD.SD	BVTV.Av	Intercept
E_{FEM}	BV/TV	0.82							1695 ($<.001$)	-62.9 (0.057)
	DTS	0.85	-3062 ($<.001$)		160 (0.002)					-283 (0.001)
	DTS+BV/TV	0.90	-1860 ($<.001$)		121 ($<.001$)				1495 ($<.001$)	-352 ($<.0001$)
									-1.39 (0.005)	0.990 ($<.001$)
VMCV	BV/TV	0.59								
	DTS	0.81		-0.03 (0.01)	-0.54 ($<.001$)	0.04 (0.04)	-8.44 ($<.001$)	12.5 ($<.001$)		1.84 ($<.001$)
	DTS+BV/TV	0.66			-0.26 ($<.001$)		-4.13 ($<.001$)		-1.11 ($<.001$)	1.58 ($<.001$)
$VMExp/\sigma_{app}$	BV/TV	0.97							-50 ($<.001$)	14.7 ($<.001$)
	DTS	0.92			-4.41 ($<.001$)		-100 ($<.001$)	134 (0.03)		18.0 ($<.001$)
	DTS+BV/TV	0.97							-50 ($<.001$)	14.7 ($<.001$)

Even though it appears that DTS parameters calculated using the aggressive binarization method had stronger and larger number of significant relationships with micro-CT parameters, DTS parameters calculated using the USM processing resulted in slightly better models of mechanical parameters than the other two processing methods. This may be because the two binarization methods produced parameters that are largely correlated to bone mass whereas the USM method produced parameters that contain heterogeneity information independent from bone mass (**Table 2**). The USM method is also a “grayscale” method which may correspond to the gray-level-based heterogeneous FE models better than the binarized images do.

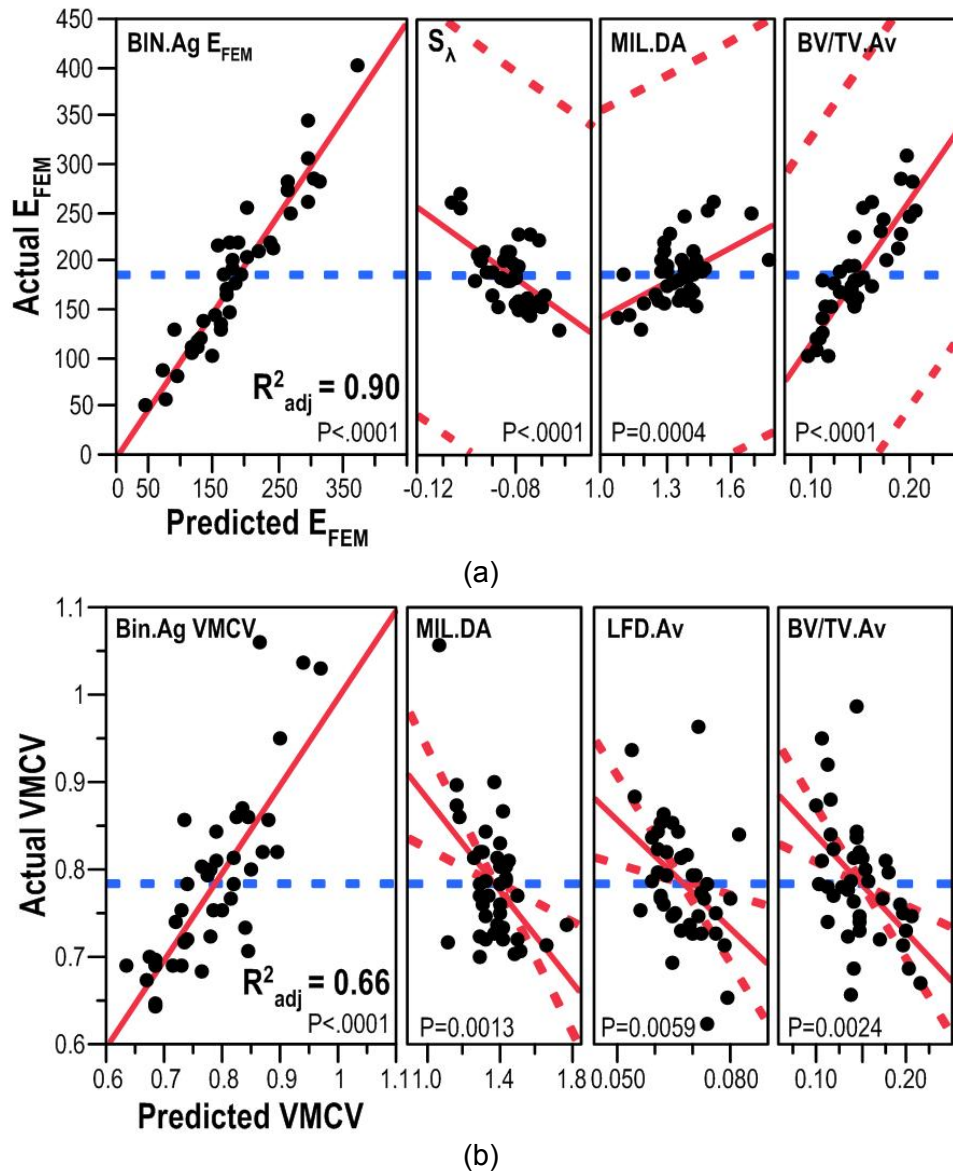


Figure 29: Multiple regression results from the aggressively binarized method (Bin.Ag). Fit of the multiple regression models constructed using both BV/TV and DTS-based predictor variables and the leverage plots for the individual effects with the associated p-values for **a)** EFEM and **b)** VMCV. The blue and the red dashed lines show the mean of the response and confidence curves, respectively.

KEY RESEARCH ACCOMPLISHMENTS

We produced strong evidence that the “concept” being explored, i.e., that quantitative analysis of bone quality using DTS is feasible.

We characterized the DTS imaging system and identified its ability to resolve features under different operational parameters.

We determined the potential of the DTS system for quantification of density.

We established methods to be used for quantitative analysis from DTS images of vertebral bone.

To the best of our knowledge, this is the first demonstration that correlates of conventionally used parameters of cancellous bone microstructure can be derived from quantitative analysis of bone texture from DTS images.

We demonstrated that parameters of cancellous bone microstructure derived from DTS increases accuracy in prediction of bone stiffness.

We designed and manufactured an innovative cost-effective apparatus that can apply multiaxial “wedge” loads using the compressive and torsional axes of a conventional materials testing machine.

REPORTABLE OUTCOMES

Manuscripts

Kim, W., Nekkanty, S., Oravec, D., Sander, E., Divine, G. W., Flynn, M. J. and Yeni, Y. N., “Digital tomosynthesis as a potential vertebral fracture risk assessment tool”

Manuscript in preparation to be submitted to Spine. A first draft is generated, under revision by the first author.

Abstracts

Kim, W., Oravec, D., Sander, E., Divine, G. W., Flynn, M. J. and Yeni, Y. N., "Digital Tomosynthesis-Derived Microstructural Parameters Predict Cancellous Bone Stiffness in Human Vertebrae"

Conference abstract submitted to the 59th Annual Meeting, Orthopaedic Research Society, January 26-29, 2013, San Antonio, Texas.

Presentations

Structural and Microstructural Considerations in Vertebral Bone Fragility, Wayne State University, Department of Biomedical Engineering, February 23, 2012.

Invited seminar as a part of a graduate class: BME seminar class (BME 8070).

Deciphering trabecular microstructure using digital tomosynthesis (DTS), Bone and Joint Center Seminar Series, Henry Ford Hospital, August 3, 2012.

Institutional level seminar. Presented by Dr. Woong Kim (a post-doctoral fellow in our group)

Funding applied for based on work supported by this award

April, 2012: “Novel Digital Tomosynthesis and Noncoding RNA Approaches to Predict Progression of Osteoarthritis”

FY12 DOD CDMRP Peer Reviewed Medical Research Program Investigator Initiated Award

Role on grant: Principal Investigator (MPI: Gibson)

The proposed project was based on the methods developed for analysis of bone quality from DTS images and the encouraging results obtained from vertebral bone. However, we were not invited to submit a full application.

Employment or research opportunities applied for and/or received based on experience/training supported by this award

This project provided training opportunities for the following individuals whether or not they were compensated by the project funds:

1. Woong Kim, PhD: University of Auckland, New Zealand, Post-doc fellow, 2012 – present.
Scanning and analysis methods for DTS imaging of vertebral bone.
2. Richard Banglmaier, PhD: Wayne State University, Senior Research Engineer, 2011-present.
Nonuniform mechanical testing of vertebral bone.
3. Daniel Oravec, MSc: Tampere University of Technology, Finland, Research Engineer, 2011 – present
All aspects of the project.
4. Ryan Bylsma, Student, Wayne State University, School of Medicine, October 2011 – January 2012.

Micro-CT scanning of bone

5. Mary Nixon, Student, Wayne State University, School of Medicine, May 2012 – July 2012.
Image processing and analysis.
6. Justin Schupbach, Student, Wayne State University, School of Medicine, June 2012 – July 2012.
Image processing and analysis.
7. Kaitlin McLoughlin, Student, Wayne State University, School of Medicine, August 2012 – September 2012.
Stereologic analysis of cancellous bone.
8. Kalyan Sreeram, Student, Wayne State University, School of Medicine, August 2012 - present.
Image processing and analysis.
9. Thomas K Maatman, Student, Wayne State University, School of Medicine, August 2012 – present.
Micro-CT scanning of bone, bone phantoms and image analysis.
10. Nicole Ramo, Student, Kettering University, Biomedical Engr., Winter 2011, Spring 2012.
Micro-CT image analysis. Specimen preparation.
11. Jason Bagnall, Student, Oakland Community College, Engineering, March – August 2012.
Micro-CT image processing. Stereologic analysis of cancellous bone.
12. Vincent Giacomelli, Student, Harrison High School, Farmington, MI, June 18 – August 10, 2012.
DTS image processing, LFD analysis of cancellous bone images.

CONCLUSION

DTS generated images analyzed by Fractal, MIL and LFD methods provided good to excellent predictions of in vitro vertebral trabecular bone stiffness and further improved the prediction ability from bone mass alone. Because cancellous bone stiffness is a strong correlate of bone strength, we expect that these methods will perform equally well for predicting bone strength and thus this technique could augment the current clinical imaging modalities (DEXA and CT) to increase the prediction accuracy of the fracture risk in patients.

As planned, future work should extend to examine the ability of DTS imaging to predict whole vertebral strength. We identified several potential approaches to improve information extraction from DTS images and these will be pursued. It also remains to be determined, in the longer term, to what extent DTS derived parameters can predict fracture risk in vivo.

REFERENCES

- Buckley, J. M., Cheng, L., Loo, K., Slyfield, C. and Xu, Z. (2007). "Quantitative computed tomography-based predictions of vertebral strength in anterior bending." *Spine* 32(9): 1019-1027.
- Fazzalari, N. L. and Parkinson, I. H. (1996). "Fractal dimension and architecture of trabecular bone." *J Pathol* 178(1): 100-105.
- Flynn, M. J., McGee, R. and Blechinger, J. (2007). Spatial resolution of x-ray tomosynthesis in relation to computed tomography for coronal/sagittal images of the knee, San Diego, CA, United states, Progress in Biomedical Optics and Imaging - Proceedings of SPIE, SPIE, 6510: 65100D-65109.
- Geraets, W. G. (1998). "Comparison of two methods for measuring orientation." *Bone* 23(4): 383-388.
- Goulet, R. W., Goldstein, S. A., Ciarelli, M. J., Kuhn, J. L., Brown, M. B. and Feldkamp, L. A. (1994). "The relationship between the structural and orthogonal compressive properties of trabecular bone." *J Biomech* 27(4): 375-389.
- Hou, F. J., Lang, S. M., Hoshaw, S. J., Reimann, D. A. and Fyhrie, D. P. (1998). "Human vertebral body apparent and hard tissue stiffness." *J Biomech* 31(11): 1009-1015.

- Kalidindi, S. R., Abusafieh, A. and El-Danaf, E. (1997). "Accurate Characterization of Machine Compliance for Simple Compression Testing." *Experimental Mechanics* 37(2): 210-215.
- Karperien, A. (2007). "FracLac for ImageJ, version 2.5." <http://rsb.info.nih.gov/ij/plugins/fractalac/FLHelp/Introduction.htm>. 1999-2007."
- Kim, D. G., Christopherson, G. T., Dong, X. N., Fyhrie, D. P. and Yeni, Y. N. (2004). "The effect of microcomputed tomography scanning and reconstruction voxel size on the accuracy of stereological measurements in human cancellous bone." *Bone* 35(6): 1375-1382.
- Kinds, M. B., Bartels, L. W., Marijnissen, A. C., Vincken, K. L., Viergever, M. A., Lafeber, F. P. and de Jong, H. W. (2011). "Feasibility of bone density evaluation using plain digital radiography." *Osteoarthritis Cartilage* 19(11): 1343-1348.
- Kuhn, J. L., Goldstein, S. A., Feldkamp, L. A., Goulet, R. W. and Jesion, G. (1990). "Evaluation of a microcomputed tomography system to study trabecular bone structure." *J Orthop Res* 8(6): 833-842.
- McDonnell, P., Harrison, N. and McHugh, P. E. (2010). "Investigation of the failure behaviour of vertebral trabecular architectures under uni-axial compression and wedge action loading conditions." *Med Eng Phys* 32(6): 569-576.
- Nekkanty, S., Yerramshetty, J., Kim, D. G., Zauel, R., Johnson, E., Cody, D. D. and Yeni, Y. N. (2010). "Stiffness of the endplate boundary layer and endplate surface topography are associated with brittleness of human whole vertebral bodies." *Bone* 47(4): 783-789.
- Plotnick, R. E., Gardner, R. H., Hargrove, W. W., Prestegard, K. and Perlmutter, M. (1996). "Lacunarity analysis: A general technique for the analysis of spatial patterns." *PHYSICAL REVIEW E* 53(5): 5461-5468.
- Reimann, D. A., Hames, S. M., Flynn, M. J. and Fyhrie, D. P. (1997). "A cone beam computed tomography system for true 3D imaging of specimens." *Appl Radiat Isot* 48(10-12): 1433-1436.
- Sander, E. A. and Barocas, V. H. (2009). "Comparison of 2D fiber network orientation measurement methods." *J Biomed Mater Res A* 88(2): 322-331.
- Whealan, K. M., Kwak, S. D., Tedrow, J. R., Inoue, K. and Snyder, B. D. (2000). "Noninvasive imaging predicts failure load of the spine with simulated osteolytic defects." *J Bone Joint Surg Am* 82(9): 1240-1251.
- Yeni, Y. N., Christopherson, G. T., Dong, X. N., Kim, D. G. and Fyhrie, D. P. (2005). "Effect of microcomputed tomography voxel size on the finite element model accuracy for human cancellous bone." *J Biomech Eng* 127(1): 1-8.
- Yeni, Y. N. and Fyhrie, D. P. (2001). "Finite element calculated uniaxial apparent stiffness is a consistent predictor of uniaxial apparent strength in human vertebral cancellous bone tested with different boundary conditions." *J Biomech* 34(12): 1649-1654.
- Yeni, Y. N., Zinno, M. J., Yerramshetty, J. S., Zauel, R. and Fyhrie, D. P. (2011). "Variability of trabecular microstructure is age-, gender-, race- and anatomic site-dependent and affects stiffness and stress distribution properties of human vertebral cancellous bone." *Bone* 49(4): 886-894.

APPENDICES

Appendix 1:

Kim, W., Oravec, D., Sander, E., Divine, G. W., Flynn, M. J. and Yeni, Y. N., "Digital Tomosynthesis-Derived Microstructural Parameters Predict Cancellous Bone Stiffness in Human Vertebrae", *Conference abstract submitted to the 59th Annual Meeting, Orthopaedic Research Society, January 26-29, 2013, San Antonio, Texas.*

Digital Tomosynthesis-Derived Microstructural Parameters Predict Cancellous Bone Stiffness in Human Vertebrae

Kim, Woong¹; Oravec, Daniel¹; Sander, Edward²; Divine, George W¹; Flynn, Michael J¹; Yeni, Yener N¹

1. Bone and Joint Center, Henry Ford Hospital, Detroit, MI, United States.
2. Dept of Biomedical Engineering, The University of Iowa, Iowa City, IA, United States.

Introduction: Clinical modalities currently available for the assessment of fracture risk in the spine largely rely on the bone mineral density (BMD) measurements; however their ability to provide information on the trabecular structure is limited. Digital tomosynthesis (DTS) is a relatively new imaging modality that has many advantages over the conventional CT and radiography, where DTS can generate multiple image slices with superior in-plane resolution than that of CT but with only 1/6th of the radiation. Nekkanty et al. have recently reported that fractal dimension (FD) as measured from DTS images of human vertebrae is correlated to stereologic measures of cancellous microstructure obtained from μ -CT images [1]. Also they have shown that FD could be used to predict the compressive stress state in the microstructure. The objectives of this study was to investigate if the MIL (mean intercept length) and LFD (line fraction deviation [2]) parameters of DTS images obtained from human vertebrae could i) be correlated to the μ -CT stereological parameters and ii) predict trabecular bone stiffness, independent from bone volume fraction.

Methods: T6, T8, T11, and L3 vertebrae from 5 female and 5 male cadavers (age 63-90yr) were μ -CT scanned and reconstructed at 45 μ m voxel size. In each trabecular bone region, mean (Av) and standard deviation (SD) of the bone volume fraction (BV/TV), trabecular thickness (Tb.Th), number (Tb.N), and separation (Tb.Sp), and degree of anisotropy (DA) were calculated. Cancellous bone apparent modulus (E) was calculated from a finite element (FE) simulation of inferior-superior compression [3]. The same bones were scanned using DTS (Shimadzu Sonalvision Safire II) and reconstructed. In each image set, the coronal central slice was used for MIL and LFD analyses (**Fig 1**). Mean (Av), standard deviation (SD), maximum (Max) and degree of anisotropy (DA) were recorded (MIL.DA = ellipse fitted Max/Min and LFD.DA = Raw Max/LFD orthogonal to Max). Mixed model regressions of μ -CT parameters to DTS parameters were examined (**Table 1**). Multi regression models were constructed to examine the relationship of MIL and LFD parameters with E with and without BV/TV. In all regression models, the donor variable was included as a random effect to account for pseudo-replication.

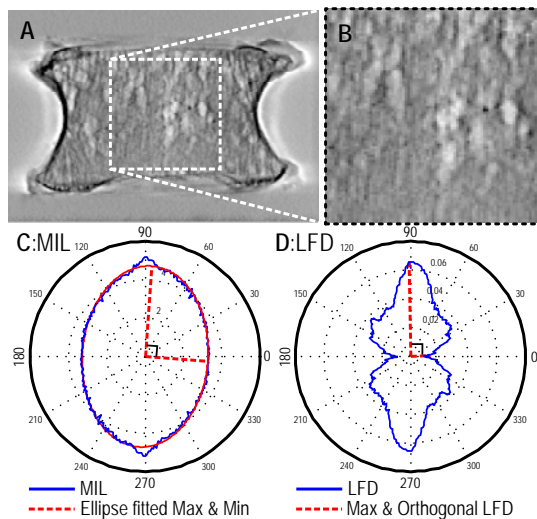


Figure 1 – [A] Coronal view of DTS image of a L3 vertebra and [B] region analyzed with [C] MIL (mean intercept length) and [D] LFD (line fraction deviation) methods. The overall alignment of MIL and LFD plots corresponds to that of the trabecular texture. Dotted red lines mark vectors of ellipse fitted max and min MIL in [C], and max LFD and orthogonal to the maximum LFD in [D].

Results: MIL.Max, MIL.DA, MIL.SD, LFD.Max and LFD.Av from DTS were significantly related with Tb.Th.Av, BV/TV.SD, Tb.Th.SD, Tb.N.SD and DA from the μ -CT stereological parameters (**Table 1**, $p < 0.001$ to $p < 0.05$). DTS parameters were significant in multiple regression models of E after accounting for BV/TV (**Fig 2**). Multiple regression models of E using DTS parameters alone (MIL.DA + MIL.Av + LFD.Max) were as predictive as BV/TV alone ($R^2_{adj} = 0.832$ vs. 0.819 respectively).

R (p-value)	MIL.Max	MIL.DA	MIL.SD	LFD.Max	LFD.Av
Tb.Th.Av		+0.82 (0.01)	+0.83 (0.01)	+0.77 (0.04)	+0.77 (0.02)
BV/TV.SD	-0.86 (0.02)				
Tb.Th.SD		+0.87 (<0.001)	+0.86 (<0.001)		+0.81 (0.03)
Tb.N.SD	-0.86 (<0.001)	-0.86 (0.01)	-0.86 (<0.001)		
DA		+0.75 (0.02)	+0.73 (0.05)		

Table 1– R of mixed linear regression of μ -CT (rows) against DTS parameters (columns). Only those with $p < 0.05$ are shown.

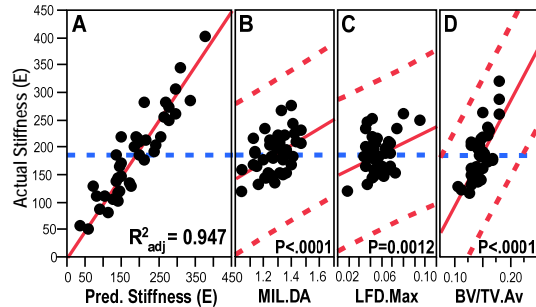


Figure 2 – [A] Actual vs. predicted stiffness plot of the multi regression model based on both DTS and BV/TV parameters. [B, C, D] The regression model's leverage plots for the individual effects (MIL.DA, LFD.Max and BV/TV.Av) with the associated p-values. The results show that stiffness prediction with the model is excellent ($R^2_{adj} = 0.947$).

Discussion: We demonstrated that correlates of the standard μ -CT stereological parameters can be obtained from DTS images using MIL and LFD methods. Also we were able to demonstrate that DTS images can be used to predict stiffness of human vertebral bone. In fact, DTS derived model performed equally well as the BV/TV-only model indicating that DTS alone is potentially as powerful a tool as those measuring BMD for predicting vertebral stiffness. When BV/TV.Av (a surrogate of bone mass) and DTS parameters were combined, the explained variability in E increased from 82% to 95%, suggesting that DTS contains trabecular structural information that is independent of BV/TV.Av and therefore it could be used as a complementary modality to DEXA and tomographic BMD measures. This in turn opens an exciting possibility that DTS can be used, not only as a qualitative imaging tool, but as a quantitative tool to assess bone fracture risk while subjecting patients with a relatively low radiation. Because cancellous bone stiffness is a strong correlate of bone strength, we expect that these methods will perform equally well for predicting bone strength. However, it remains to be determined to what extent DTS derived parameters can predict whole bone strength and fracture risk in vivo.

Significance: DTS generated images analyzed by MIL and LFD methods provided good to excellent predictions of in vitro vertebral trabecular bone stiffness and thus this technique could augment the current clinical imaging modalities (DXA and CT) to increase the prediction accuracy of the fracture risk in patients.

Acknowledgements: DOD PRMRP W81XWH-11-1-0769 and NIH AR059329.

References: [1] Nekkanty et al., 2011, 57th ORS, p. 670. [2] Geraets, W. 1998, Bone, 23(4): p. 383-388. [3] Yeni et al, 2011, Bone, 49: 886-94.